COPPE
UFRJ

Instituto Alberto Luiz Coimbra de
Pós-Graduação e Pesquisa de Engenharia

ANALYSIS OF DYNAMIC COMPRESSIVE FRACTURE OF CARBON COMPOSITES BY DIGITAL IMAGE CORRELATION

Rafael de Azevedo Cidade

Tese de Doutorado apresentada ao Programa de Pós-graduação em Engenharia Metalúrgica e de Materiais, COPPE, da Universidade Federal do Rio de Janeiro, como parte dos requisitos necessários à obtenção do título de Doutor em Engenharia Metalúrgica e de Materiais.

Orientador: Enrique Mariano Castrodeza

Rio de Janeiro
Maio de 2019

ANALYSIS OF DYNAMIC COMPRESSIVE FRACTURE OF CARBON COMPOSITES BY DIGITAL IMAGE CORRELATION

Rafael de Azevedo Cidade

TESE SUBMETIDA AO CORPO DOCENTE DO INSTITUTO ALBERTO LUIZ COIMBRA DE PÓS-GRADUAÇÃO E PESQUISA DE ENGENHARIA (COPPE) DA UNIVERSIDADE FEDERAL DO RIO DE JANEIRO COMO PARTE DOS REQUISITOS NECESSÁRIOS PARA A OBTENÇÃO DO GRAU DE DOUTOR EM CIÊNCIAS EM ENGENHARIA METALÚRGICA E DE MATERIAIS.

Examinada por:

<div style="text-align:right">

_____

Prof. Enrique Mariano Castrodeza, D.Sc.

_____

Prof. Célio Albano da Costa, Ph.D.

_____

Prof. Hector Guillermo Kotik, Ph.D.

_____

Prof. José Roberto Moraes D'Almeida, Ph.D.

_____

Prof. José Xavier, Ph.D.

</div>

RIO DE JANEIRO, RJ – BRASIL
MAIO DE 2019

In memory of professor
Fernando Luiz Bastian.

Acknowledgements

ANÁLISE DA FRATURA DINÂMICA EM COMPRESSÃO EM COMPÓSITOS DE CARBONO PELA CORRELAÇÃO DIGITAL DE IMAGENS

Rafael de Azevedo Cidade

Maio/2019

Esta tese propõe o uso da técnica da correlação de imagens na análise da fratura dinâmica em compressão de compositos reforçados por fibras de carbono (IM7-8552). Imagens de testes de impacto de corpos de prova bi-entalhados foram analisadas. Também é proposto um método para determinação do tamanho dos subsets baseado nos padrões de speckle. A tenacidade a fratura dinâmica foi definida como a taxa de liberação de energia no momento de carga máxima, durante o ensaio, e foi calculada por meio de uma integral-J extendida, no domínio de área. A comparação entre os resultados das integrais área e contorno é apresentada e mostra quea integral de área é um método mais robusto quanto aos parâmetros do método, apresentando uma discrepância máxima de 14 % entre os resultados. Uma rede neutra artificial foi usada para calcular a influência relativa dos parâmetros. Os resultados não apresentaram consistência satisfatória entre amostras da mesma classe, mas mostram, em certo nível, concordância com resultados encontrados pelo grupo de pesquisa utilizando a metodologia da *size-effect law*. Além disso, uma nova metodologia é proposta, utilizando redes neurais convolucionais para prever o início da fratura por meio dos campos de tensão. Um estudo de caso para espécimes da classe III mostra que uma metodologia incluindo redes neurais convolucionais pode ser desenvolvida como uma alternativa à hipótese de carga máxima.

Abstract of Thesis presented to COPPE/UFRJ as a partial fulfillment of the requirements for the degree of Doctor of Science (D.Sc.)

Rafael de Azevedo Cidade

May/2019

Advisor: Enrique Mariano Castrodeza

Department: Metallurgical and Materials Engineering

This thesis proposes the use of digital image correlation technique on the analysis of dynamic compressive fracture of carbon fibre reinforced composites (IM7-8552). Impact tests images of double edge notched specimens were analysed. A method for determining the subset size base on morphological aspects of the speckle pattern is presented. The dynamic fracture toughness was defined as the the energy release rate at the peak load, during the test, and was calculated by an extended J-integral over an area domain. The comparison between area and contour domain integrals results is also presented and shows that the area domain is a more robust method regarding the method parameters, showing a maximum of 14% discrepancy amongst results. An artificial neutral network was used to calculate the relative influence of the parameters. The results did not present satisfactory consistency amongst specimen of the same types, yet show, in a certain level, agreement with those found by the research group by using the size-effect law methodology. In addition, a novel methodology is proposed, utilising convolutional neural networks to predict the fracture initiation by the stress fields. A case study for type III specimens shows that a methodology including convolutional neural networks can be developed as an alternative to the peak load assumption.

Contents

List of Figures

List of Tables

List of Symbols

E_i — Elastic modulus in direction i

G_{ij} — Shear modulus in direction ij

ν_{ij} — Poisson coefficient in direction ij

X_T, Y_T — Longidutinal and transverse tensile strength

a_0 — Initial notch length

W — Specimen half width

$D, D_{\%95}$ — Speckle diameter and 95% of speckles diameters distribution

SR — Subset radius

NND — Nearest neighbour distance and 95% of nearest neighbour distance distribution

ϵ — Strain tensor

$u, \dot{u}, \ddot{u}$ — Displacement, velocity, and acceleration vectors

P, P^n — Savitzky-Golay filter polynomial and n^{th} derivative

C — Savitzky-Golay filter polynomial coefficients

$w, w_c, \dot{w}$ — Work, work on crack vicinity, and work flux

$T, \dot{T}$ — Kinetic energy and kinetic energy flux

$a, \dot{a}$ — Crack size and speed

$G^{dyn}\tilde{G}_A, \tilde{G}_\Gamma$ — Dynamic energy release rate and discrete implementation for area and contour domain

G — Critical energy release rate

R — Crack resistance curve

t — Stress vector

Γ — Closed contour integration domain

A — Area integration domain

U — Strain energy

ρ — Material density

γ_i — Inner closed contour around crack tip

q — Weight function

c, h — Domain width and height

dp — Data point

f, f_p — Frame and frame at peak-load

σ_u — Peak-load normalised by SHPB cross-section area (peak-stress)

SW — Strain window

ϕ — Geometric correction factor

α — crack size normalised by specimen half width

Chapter 1

Introduction

Composite materials have been gradually replacing traditional metallic materials in their customary applications over the past decades. Therefore, the demand for their proper understanding, characterisation, and modelling has risen and new experimental and computational techniques have been developed. [1].

This trend is noticeable in aerospace, automotive and marine industries, including offshore oil production, where composite materials have been gaining more importance either in usage as in research and development. In such cases, structures are subjected to multiple loads, leading to complex stress states either static or dynamic. Therefore the accurate design and prediction of life in service is of great importance, in order to minimise life and environment risk.

The complexity of composite materials starts in their very basic intrinsic properties, their constitutive relation. Differently from the widely used and studied metallic materials, which present fully symmetry, or isotropy, fibre reinforced materials are generally orthotropic materials, or in some cases present transverse isotropy. It means that, instead of having only two properties to describe their elastic behaviour, more constants are needed. The same applies for strength limits and fracture toughness parameters, where not only the magnitude and direction matter, but also the sign.

Besides geometric complexities, time also comes into scope. Such materials could present, for some directions, loading rate sensitiveness, that is, the constitutive relation varies as the loading scenario goes from static to dynamic. It applies not only for the constitutive relation but also for strength limits and fracture toughness. For many years researchers have dedicated their studies to better understand the rate sensitiveness and no consensus has been reached, what makes this subject still open for future researches.

The fracture toughness is one of the key variables for the understanding and

---

[1]in this document *composite materials refers to fibre reinforced polymers*

1

predicting failure in composite materials, its proper assessment and modelling are of great importance on risk mitigation and in service failure estimates. Allied to the time sensitivity that such materials could present, it makes necessary not only to test it under quasi-static scenarios, but also along a wide range of dynamic loads.

The objective of this thesis is to primarily assess the mode I fracture toughness of carbon fibres composites subjected to high compressive loading rates, suggesting a computational strategy for data reduction based on digital image correlation (DIC) and machine learning techniques. It evaluates the method robustness, regarding its parameters as well as the energy components involved in the dynamic fracture process. Additionally a parallel study is done on image classification of full field measurements by convolutional neural networks in a essay (try) to predict, by machine learning, the time to fracture base on the stress fields.

Scope

The scope of this document is summarised as follows:

i Assessment of mode I intralaminar fracture toughness of carbon composite under compression

ii Determination of full field measurements and its time derivatives

iii Calculations of fracture toughness by an extended J-Integral over full-field measurements

iv Use of artificial neural networks as an alternative of ANOVA table for variables relative influence

v Time to fracture estimates by convolutional neural networks training over stress fields

The following points are out of the scope of this thesis:

i The experimental setup. It is out of the scope of this thesis the discussion of experimental set up parameters, as well as equipment configurations.

ii The derivation and implementation of the digital image correlation technique. In this study the open source implementation, Ncorr[1], was used for DIC calculations.

ii The implementation of artificial neural networks. The concern about artificial neural networks in the present work are the proper choice of architecture and suitable input data.

1.1 Thesis organisation

This thesis is organised in the following sections:

Chapter 2 presents a review of the state of the art regarding the dynamic fracture mechanics of composite materials. This section sorts the referenced works into three different categories, according to the studied mode: mode I, mode II, and mixed mode, presenting the experimental apparatus as well as the data reduction methods. In addition it presents a review of related works based on DIC fracture mechanics studies.

Chapter 3 is divided into five sections. Section 3.1 approaches the experimental setup, specimens preparation and data acquisition methodologies, explaining all the process of generating input data from dynamic tests on the SHPB for post processing and further analysis. Section 3.2 discuss the use of DIC on generating full-field measurements of displacements and its derivatives (i.e. strains, velocities, and acceleration).It is (also) proposed here an algorithm, or a set of steps and parameters, for enhancing accuracy of DIC calculations as well. In section 3.3 is presented the J-integral formulation and the derivation of the modified equation used in this thesis. It is also explained the discrete implementation over full-field data, discussing the influence of calculation parameters such as the domain size on J-integral value. Section 3.3.3 is a comparative study between the the present work and the assumption of a rising R-curve for the analysed material, (found) reported in literature. Lastly, section 3.3.4 explores convolutional neural networks as a method for identifying fracture initiation based on stress fields.

Chapter 4 presents the results related to sections cited above. This chapter discusses the influence of each parameters of the process on the final J-integral value and compares the calculated fracture toughness value to results found in literature. It is also shown a case study where the use of trained convolutional neural networks would predict the fracture initiation in the absence of load measurement during the test.

1.2 Related Publication

Cidade, R. A., Castro, D. S. V., Castrodeza, E. M., Kuhn, P., Catalanotti, G., Xavier, J., Camanho, P. P. (2019). *Determination of mode I dynamic fracture toughness of IM7-8552 composites by digital image correlation and machine learning.* Composite Structures, 210, 707-714.

Chapter 2

Literature review

KANNINEN e POPELAR [2] divide dynamic fracture toughness problems in two categories [1]:

   i Rapidly varying applied load;

  ii Quasi-static loads and rapidly moving crack.

Owing to the purpose of these study (i.e. high strain-rate applied to carbon fibre composite specimens), most attention will be given to the first case.

JACOB *et al.* [4] published an article attempting to review all existing publications about the strain rate dependence on mode I, mode II, and mixed mode fracture toughness of composite materials comprising works between 1985 and 2001. They noticed a lack of consensus about the effects of strain-rate in the fracture toughness of composite materials. Not only for mode I, but also for mode II, and for mixed-mode. No major conclusions could be drawn about the strain-rate dependence even in cases with similar materials under common strain-rate ranges. In spite of not finding a trend, three concluding remarks were made:

   i Dynamic fracture toughness depends basically on the matrix properties, what are rate-dependent;

  ii A ductile-brittle transition may occur as the rate increases reducing the composite fracture toughness.

 iii Referenced authors show great concern on experiments preparation due to procedure related sensitivity.

This section aims to review recent works related to dynamics fracture mechanics of composite materials[2] and the strain-rate dependence of dynamic fracture toughness, as well as the data reduction strategies presented.

---

[1] A similar classification is also found in ANDERSON [3]

[2] fibre-reinforced polymer.

2.1 Mode I

FRACASSO *et al.* [5] studied the mode I dynamic delamination of double cantilever beam (DCB) Carbon/PEEK specimens, with interleaved plies, under 0.5, 10, and $200mm/min$ rates at temperatures from $23°C$ to $120°C$. Using the time-temperature equivalence postulate, they obtained a master curve of the fracture toughness for a wide range of crack speeds. They reported a reduction about 58% of interlaminar fracture toughness with the increase of crack speed, which was approximately constant during each the tests. The authors also concluded that interleaving does not change the trend of fracture toughness rate dependence.

SUN e HAN [6] proposed a novel method to asses the mode I dynamic delamination in polymeric composites. They conducted wedge-insert-fracture (WIF) tests with wedge loaded compact tension (WLCT) specimens using a split Hopkinson pressure bar (SHPB) to achieve high strain-rates in carbon/epoxy and glass/epoxy specimens. They also used a MTS machine at a 0.01 mm/min cross-head rate to obtain quasi-static results. Fracture toughness was calculated by finite elements model using the modified crack closure (MCC) method. They simulated the dynamic delamination by sequentially removing the boundary conditions, releasing the nodes placed at the symmetry plane (crack plane), based on measured crack speed and load history. The glass/epoxy dynamic crack initiation toughness was higher than the quasi-static. According to the authors, it may have occurred due to more severe fiber bridging under dynamic loading compared to the quasi-static test, which made difficult the measurement of toughness during crack propagation. On the other hand, carbon/epoxy initiation toughness was rate insensitive to crack speeds up to $900m/s$.

WU e DZENIS [7] investigated the dynamic mode I interlaminar initiation toughness of a unidirectional carbon/epoxy composite (P7051S-20Q-1000). They performed impact tests using a Hopkinson pressure bar with a modified three point bend specimen (1-bar/3PB) with striker impact speeds about $20-30m/s$ $(23-53J)$. They noticed that the supporting fixture constrained the specimen after crack initiation, causing a complicated reflected wave shape . But it was also noticed that the crack initiation occurred at the beginning of the impact event, therefore the data reduction took in account only the initial part of the reflected wave signal. The dynamic stress intensity factor (DSIF) was calculated using a two-dimensional finite elements analysis with implicit method, due to the smooth loading history. They reported that the critical DSIF, for the transient loading presented on their study, is about 80-90% of the static value. In addition, they concluded, based on fracture surfaces, that dominant failure mechanisms were matrix brittle failure and fiber/matrix debonding.

BLACKMAN *et al.* [8, 9] assessed quasi-static and dynamic fracture toughness of a rubber-toughened epoxy adhesive using double cantilever beam (DCB) and tapered double cantilever beam (TDCB) tests. Two different substrates were used to manufacture the joints: An aluminum alloy (EN AW-2014) and an unidirectional carbon composite (HTS/6376). Tests were performed from quasi-static ($0.1mm/min$) to dynamic ($15m/s$) regimes using both a screw driven and a servo-hydraulic machine, using a high-speed camera to monitore the crack growth. The results were divided into four categories[3]:

$$
\text{Quasi-static} = \begin{cases} \text{Type 1: Stable and continuous crack growth} \\ \text{Type 2: Unstable, stick-slip, crack growth}(10^{-2}m/s) \end{cases}
$$

$$(2.1)$$

$$
\text{Dynamic} = \begin{cases} \text{Type 3: Unstable, stick-slip, crack growth}(2.5m/s) \\ \text{Type 4: Stable and continuous crack growth}(12m/s) \end{cases}
$$

$$(2.2)$$

The results show that the fracture type evolves, subsequently, from type 1 to type 4 as the load-rate increases. In the dynamic case, the authors reported a decrease of about 40% of the quasi-static value, possibly caused by the inability of the material to rapidly dissipate the heat generated at the crack tip.

JOUDON *et al.* [10] tested a toughened resin epoxy (Hexply® M21), widely used in aeronautical composites, for dynamic fracture toughness measurements, using single-edge notched bending (SENB) specimens. The tests were performed in a servo-hydraulic machine under displacements rates from $5mm/min$ to $20m/s$ using a high speed camera to monitor the crack growth. The dynamic fracture toughness was calculated using a strain-gage technique base on the local analysis of the asymptotic strain field, assuming constant propagation speed. The authors reported that the dynamic stress intensity factor can exceed the quasi-static initiation toughness in about 25% under higher crack speeds scenarios ($293m/s$).

NAVARRO *et al.* [11] investigated the influence of crack speed on mode I delamination fracture toughness of woven composites using double cantilever beam specimens manufactured in eight different stacking sequences comprising glass fibers fabric (Hexcel 913/45%/7781) layups, carbon fibers fabric (Hexcel 913/45%/G963) layups and hybrid configurations. The tests were performed in a drop weight tower, delivering impacts of $4m/s$. For each stacking sequence, they used specimens with different lengths of internal adhesive layer (at crack plane) in order to asses a wider range of crack speeds. Experimental data show no influence of crack speed on mode

---

[3]The values in parenthesis indicate the transition test rate to the specified type

I fracture toughness and no evidence was found on fractographic analysis. The authors allege that experimental data are in accordance with previous studies since increases in fracture toughness would occur for crack speeds higher than $1000m/s$, which was not reached in their study.

ZABALA *et al.* [12] performed DCB tests on unidirectional (Toray's Ref. GV 170U) and woven (Hexcel Ref. 43199) carbon/epoxy (SiComin RS 8100/SD 8822) composites containing 19% of E-Glass fiber, in transverse direction, in order to keep the carbon fibers together during the manufacturing process. In addition, transversal glass fibers reduce the interactions between adjacent carbon fibers plies, which is useful to avoid fiber bridging. The fiber bridging phenomenon is particular to unidirectional composite specimens, not reflecting the behavior of an actual structure, and should be avoided on strain-rate dependence analysis (CANTWELL e BLYTON [13], REEDER *et al.* [14]). The tests were conducted in a servo-hydraulic machine from quasi-static ($8.3 \times 10^{-3}m/s$) to dynamic ($0.19m/s$) rates and the crack, measured by digital image correlation using a high speed camera. The results show a linear descending trend of the fracture toughness as a loading rate function and the propagation characterised as unstable. At the highest loading-rate a reduction of 19% of G_{IC} was reported for the woven specimens and 32% for the unidirectional composites in relation to the quasi-static tests.

BEDSOLE *et al.* [15] studied the mode I dynamic fracture toughness of carbon/epoxy specimens with neat resin as well as with carbon nanotubes filled matrix. They performed quasi-static 3PB tests using a electromechanical testing machine (under 0.01mm/s) and dynamic 1PB (one point bending) impact tests using a Hopkinson bar, achieving crack speeds around 800m/s. Two specimens configurations were used in order to assess both interlaminar and intralaminar dynamic fracture toughness. The results show increases of approximately 155% and 113% for interlaminar fracture toughness of the neat resin and the carbon nanotubes specimens respectively when compared to the quasi-static tests. For the dynamic intralaminar case, the increases were around 153% and 190% respectively, when compared to the quasi-static tests.

KUHN *et al.* [16, 17] tested double edge notched specimens under both tension and compression for mode I intralaminar fracture toughness. The tests were conducted in a SHPB, under strain rates of $60s^1$ and $100s^{-1}$ respectively. For the tensile case increases up to 28% were reported compared to the quasi-static results, while under compression, the material responded with higher sensitivity, 60% when compared to the quasi-static value.

2.2 Mode II

FRACASSO *et al.* [5] also studied the rate dependence on mode II delamination. Using an end notch flexural (ENF) carbon/PEEK specimen they tested the material under 0.5, and $10mm/min$ regimes. Analog to mode I, the used the time-temperature postulate to build a master curve for a wide range of crack speeds. Therefore, they performed the tests at temperatures from $23°C$ to $160°C$. It was reported a a non-monotonic trend for fracture toughness with a maximum occurring at a crack speed of $10^{-13}m/s$, suggesting a change in fracture mechanism, but no supporting evidence was found in fracture surface images.

WOSU *et al.* [18] performed two-bars / three point bending (2-bar/3PB) tests, with the use of a split hopkinson pressure bar, to evaluate the dynamic energy release rate, under pure mode II loading, of carbon/epoxy end-notched flexural (ENF) and centre-notched (CNF) specimens. They stated that the use of long bars and short specimens can assure the assumption of dynamic equilibrium and uniform stress field. The energy release rate (G_{II}) was estimated by a closed form solution based on the beam theory, as a impact energy function. The authors observed an increase of G_{II} with the impact energy and suggested a power law model to fit experimental data. Regarding the different specimens used on their study, they noticed some differences:

   i CNF showed greater stress values after first reflection and smaller transmitted signal than ENF.

   ii ENF experienced a higher load than CNF for the same impact energy.

   iii CNF exhibited a compressive strength 46% higher than ENF.

Therefore, it was concluded that a crack at the edge of a structure leads to a lower strength compared to a structured with an internal crack. Furthermore, as JACOB *et al.* [4] previously mentioned, they pointed out the inconsistencies between some authors on the trend of dynamic fracture toughness as a strain-rate function and they attribute this to inaccurate measures or estimates of the actual stress field at the crack tip and suggest the use of embedded fiber Bragg gratings for proper strain measurement.

COLIN DE VERDIERE *et al.* [19] investigated the dynamic Mode II delamination of Non-Crimp Fabric (NCF) carbon/epoxy composites using end loaded split (ELS) specimens mounted on a drop tower . Two different NCF composites were tested: untufted (standard) and tufted. Quasi-static tests were also performed to evaluate the loading-rate dependence. The crack-displacement response was calculated by image analysis using a high speed camera. They noticed that in tufted

specimens the crack grows more stable, reaching a maximum speed of $18.0m/s$, compared to the untufted specimens, with speeds up to $130m/s$. The results show no rate dependence on fracture toughness for the standard specimens and slight positive influence, attributed to friction generated by broken tufts. Regarding the method employed, the authors reported a lack of accuracy on load acquisition during the crack propagation due to great signal oscillation, making difficult the calculation of G_{IIc} based on load measurements. Instead, they used the crack-displacement response combined with specimen geometry and flexural properties. They also suggest the use of SHPB as an alternative method, in order to produce less load signal oscillation at high speeds, since the calculation takes in account the transmitted bar strain.

In addition to their work on mode I [8], BLACKMAN *et al.* [9] performed end-notch flexure tests on unidirectional carbon composite joints to investigate the rate effect on mode II fracture energy. They performed the tests under displacement rates of $0.1m/s$, $1m/s$, and $10m/s$, using a high speed camera do measure the deformation. Their results show unstable cohesive fracture for all specimens and no sensitivity to the testing rate.

2.3   Mixed Mode

WOSU *et al.* [20] proposed a mixed-mode opening notch flexure (MONF) test to assess the dynamic mixed-mode delamination fracture toughness of carbon/epoxy (AS4/3501-6) specimens. They used a SHPB with a two-bar/three point bending setup to generate the stress wave with impact energies in a range from 1.0 to 9.3J. The desired mixed-mode ratio (G_I/G_{II}) was achieved by varying the loading-point position along the specimen span (e.g. pure Mode I is achieved when the load is applied at specimen midspan). Energy release rate was calculated by a closed form modified beam analysis that takes in account the transverse shear and the rotation at crack tip. The results show that the dynamic fracture toughness increases non-linearly with absorbed energy for all mode ratios ($G_I/G_{II} = \{1.333, 0.374, 0.076, 0.015\}$).In addition, the authors say that the slow progress in developing dynamic fracture toughness tests and the lack of experimental data are related to difficulties such as:

   i Accurate determination of the loading-point displacement;

   ii Measurement of the crack tip speed at high strain rates;

   iii Development an accurate closed form model;

   iv Reliability on specimen configuration to be used in impact tests.

LEE *et al.* [21] performed quasi-static and dynamic tests to evaluate intralaminar mixed-mode fracture toughness of unidirectional carbon/epoxy (T800/3900-2) single-edge notched specimens. To the former case they used an electromechanical testing machine with a cross-head speed of $4 \times 10^{-3} mm/s$ while the latter was performed using a drop tower with impact velocity of $4.8 m/s$, achieving crack speeds up to $560 m/s$ Different orientation angles were used to produce mixed-mode fracture. The displacement field was obtained using digital image correlation (DIC). The fracture toughness was subsequently calculated using a continuum based linear elastic fracture mechanics approach, assuming macroscopic homogeneity and material orthotropic behavior. The authors reported an upward trend in crack initiation toughness with the loading-rate. In addition they observed an exponential decay behavior of the fracture toughness as a function of the degree of anisotropy (longitudinal to transversal modulus ratio).

BLACKMAN *et al.* [9] also performed mixed mode tests using mixed mode flexural specimens ad the same rates as for mode II. For this case no cohesive fracture has been reported, only delamination, therefore no conclusions could be drawn.

BIE *et al.* [22] assessed the dynamic fracture toughness of carbon nanotubes/epoxy (CNT) composites and neat epoxy specimens under impact loading using the flyer plate technique. Since there is no explicit information about the fracture mode, the fracture toughness is assumed to be the sum of the individual modes and was calculated by an energy balance analysis. Due to the high strain-rate technique used, the authors reported strain-rates up to $10^6 s^{-1}$. For the neat resin specimen, an increase of 6 times the quasi-static value was found, but no quantitative information was given for the reinforced specimens.

Summary

Following there is a summary of referenced works, cited above, highlighting the materials used, the experimental procedure, and a brief conclusion.

Author	Material	Test	Rate	Dependence
FRACASSO *et al.* [5]	Carbon/PEEK	DCB	$0.5 - 200mm/min$	Reduction of 58% of the quasi-static value with increasing crack speed.
SUN e HAN [6]	Carbon/Epoxy and Glass Epoxy	WIF and WLCT using SHPB (dynamic) and MTS (quasi-static)	up to $900m/s$*	Carbon/epoxy was rate insensitive while glass/epoxy presented a higher value compared to the quasi-static case.
WU e DZENIS [7]	Carbon/Epoxy	1-bar/3PB	$20 - 30ms/s$ $(23 - 53J)$**	Dynamic fracture toughness reduced to 80-90% of quase-static value
BLACKMAN *et al.* [8, 9]	Rubber-toughened epoxy adhesive	DCB and TDCB using a servo-hydraulic machine	$0.01 - 15m/s$	Dynamic fracture toughness decreased to 40% of the quasi-static value.
JOUDON *et al.* [10]	Toughened epoxy resin	SENB using a servo-hydraulic machine	$0.005 - 20m/s$ (crack speeds up to $293m/s$)	Dynamic value increased about 40% compared to the quase static value.
NAVARRO *et al.* [11]	Carbon/Epoxy, Glass/Epoxy and hybrid composites	DCB using a drop-weight tower	$4m/s$**	No dependence has been found.
ZABALA *et al.* [12]	Carbon/Epoxy	DCB using a servo-hydraulic machine	$0.0083 - 0.19m/s$	Reduction of 19% of quasi-static value for woven and 32% for unidirectional specimens.
BEDSOLE *et al.* [15]	Carbon/Epoxy (neat and carbon nanotubes filled resin)	1PB using HPB	$800m/s$*	Increase of 155% and 113% (neat and filled) on interlaminar toughness and 153% and 190% (neat and filled) on intralaminar fracture toughness.
KUHN *et al.* [16, 17]	Carbon/Epoxy	1PB using HPB	$800m/s$*	Increase of 155% and 113% (neat and filled) on interlaminar toughness and 153%

*Crack speed

**Impact speed (Impact energy)

Table 2.1: Summary of reviews papers regarding Mode I dynamic fracture toughness.

Author	Material	Test	Rate	Dependence
FRACASSO *et al.* [5]	Carbon/PEEK	ENF	$0.5 - 10 mm/min$	Rate dependence with a non-monotonic trend. A maximum occurs at a crack speed of $10^{-13} m/s$.
WOSU *et al.* [18]	Carbon/Epoxy	ENF and CNF using 2-bar/3PB	up to $\approx 80 J$*	Increasing G_{IIC} with impact energy. The authors suggested a power law to fit experimental data.
COLIN DE VERDIERE *et al.* [19]	NCF carbon/epoxy (tuffed and untuffed)	ELS specimens mounted on a drop-weight tower	$18 m/s$** (tuffed) and $130 m/s$** (untufted)	No dependence has been noticed on tufted specimens and a slightly positive influence on tufted specimens.
BLACKMAN *et al.* [9]	UD Carbon/Epoxy joints	End-notch tests	$0.1, 1.0,$ and $10 m/s$	No dependence has been noticed

*Impact energy

**Cack speed

Table 2.2: Summary of reviews papers regarding Mode II dynamic fracture toughness.

Author	Material	Test	Rate	Dependence
WOSU *et al.* [20]	Carbon/Epoxy	MONF using a 2-bar/3PB	$1.0 - 9.3J*$	Nonlinear increasing trend of dynamic fracture toughness with absorbed energy for all studied ratios.
LEE *et al.* [21]	Carbon/Epoxy	SEN using electromechnical machine (quasi-static) and drop-weight tower (dynmic)	$4.3 \times 10^{-6} - 4.8m/s$ (Crack speeds up to $560m/s$)	Upward trend of fracture toughness as a loading-rate function.
BLACKMAN *et al.* [9]	UD Carbon/Epoxy joints	Mixed mode flexural tests	$0.1, 1.0,$ and $10m/s$	Inconclusive, no cohesive fracture was reported
BIE *et al.* [22]	CNT/Epoxy and neat resin	Flyer plate technique	Crack speeds up to $10^6 s^{-1}$	Neat resin presented a six times increase of dynamic toughness compared to quasi-static value. No quantitative information about reinforced specimens.

*Impact energy

Table 2.3: Summary of reviews papers regarding Mixed-Mode (I+II) dynamic fracture toughness.

2.4 Data Reduction

Several authors rely on quasi-static approaches on their dynamics analysis, assuming that dynamic stress equilibrium has been reached. JIANG e VECCHIO [23] shows that the quasi-static theory is the preferred method to calculate fracture toughness under impact conditions. On the other hand, NISHIOKA [24] says that the use of computer simulations is the only possible way to overcome difficulties in acquiring higher-order dynamic properties along a transient loading history.

In this section are listed the data reduction schemes used by authors cited on previous section, comprising quasi-static closed form solutions, asymptotic fields assumptions, and contour integrals methodologies.

FRACASSO *et al.* [5] used the modified beam theory method to calculate the mode I energy release rate of double cantilever beam specimens following the quasi-static approach presented on ASTM D5528 [25], even though the standard alerts that dynamic effects are not taken into account and their interpretation are beyond the scope of the standard. ZABALA *et al.* [12] followed the same scheme on dynamic mode I interlaminar energy release rate. Similarly, they used a quasi-static closed-form equation for mode II energy release rate calculation.

The same approach was used by WOSU *et al.* [18] and COLIN DE VERDIERE *et al.* [19] to calculate the mode II energy release rate. In their later study, on mixed mode delamination, WOSU *et al.* [20] used two different data reduction schemes: The first strategy is similar to their previous work on mode I delamination, using a closed form equation based on the modified beam theory for quasi-static case. The second one is derived from the energy balance of an elastic body with free ends under dynamic crack growth and takes into account the elastic energy, the fracture energy, and the kinetic energy. The specimen is considered to be under uniform stress state and the crack resistance curve, constant. The energies were calculated using the stress waves (incident, reflected, and transmitted) measured by strain-gages mounted on the two bars - three point bending SHPB configuration. They concluded that for impact energies below a threshold level ($9.3J$) the kinetic energy term could be neglected.

SUN e HAN [6] used the modified crack closure (MCC) integral to calculate mode I dynamic energy release rate of wedge loaded compact tension(WLCT) specimens mounted on a split Hopkinson pressure bar. The finite elements implementation follows the formulation suggested by JIH e SUN [26] were the inertia effects are characterized by a lumped-mass and plane-strain is assumed. The crack propagation is simulated by sequentially releasing the crack path nodes, based on experimental measurements of crack tip position, and the crack-closure integral calculated continuously trailing the crack-tip (MALLUCK e KING [27]). In addition, for JIH e SUN

[26], an advantage of this method compared to the J-Integral is that it can easily separate the energy release rate for each fracture mode without knowing, *a priori*, the mixed-mode ratio.

NAVARRO *et al.* [11] followed the work of GUO e SUN [28], which similarly to SUN e HAN [6], used the finite elements method with node releasing strategy to calculate mode I dynamic fracture toughness of carbon/epoxy and glass/epoxy composites. Differently from JIH e SUN [26], they used the energy balance (total strain-energy and total kinetic-energy) for calculating the energy release rate.

WU e DZENIS [7] also performed finite elements simulations on their dynamic delamination (Modes I and II) study. Instead of using a contour integral, like in the work presented by SUN e HAN [6], they calculated stress intensity factors directly by the COD (crack opening displacement), assuming an asymptotic displacement field near crack tip (SIH *et al.* [29]). Transient finite elements simulation was performed based on load history and time to fracture, obtained experimentally. The use of COD instead of *J*-Integral was justified by the fact that the numerical differentiation step would reduce the accuracy of the analysis, since the stress field is calculated by the displacements derivative. In addition, they say that the dynamic path-independent integral would not avoid the singular stress field because it involve area integrals within the contour.

BLACKMAN *et al.* [8, 9] relied on a quasi-static strategy employing the corrected beam theory while the dynamic analysis counted on a load-independent approach including kinetic energy effects (BLACKMAN *et al.* [30]). They also proposed an isothermal-adiabatic transition model to take in account the adiabatic heating in the vicinity of the crack tip, which they allege to cause the rate-dependence.

LEE *et al.* [21, 31] used the analytical expressions of the displacement field derived by LIU *et al.* [32] to calculate the dynamic stress intensity factor. Differently from WU e DZENIS [7], where finite elements method was employed do calculate the crack opening displacement, they used 2D DIC and high speed photography to obtain the full-field displacements and further calculate the dynamic stress intensity factors. An analogous approach was used by JOUDON *et al.* [10] for measurement of the dynamic mode I fracture toughness of toughened epoxy resins. They used a strain gage method instead of DIC, following the work of KHANNA e SHUKLA [33], which assumes an asymptotic strain field near the tip of a moving crack with constant velocity. In addition the authors mention that the local analysis of asymptotic fields are preferred on determining fracture mechanics parameters during fast propagating cracks on brittle polymers. BIE *et al.* [22], in their study on fracture toughness of carbon nanotubes/epoxy composites under impact loading, used an expression derived by GRADY [34], based on the energy balance, in their work on spall in brittle solids.

BEDSOLE *et al.* [15] followed the same approach as WU e DZENIS [7], using the analytical expression for asymptotic displacement fields (SIH *et al.* [29]) for both intralaminar and interlaminar tests, prior do crack initiation, for SIF calculation. For each pair of images (i.e. each computed displacement field) they performed a least-squares analysis to extract K_I and K_{II} , by fitting the measured displacement fields against the analytical model. Among their conclusions are the advantages of DIC technique on fracture mechanics such as crack tip precise location and non-contact measurements.

KUHN *et al.* [16, 17] used a quasi-static approach to calculate the R-curve of double edge notched compressive and tensile specimens, relying on BAŽANT e PLANAS [35] size-effect statement, that means, geometric similar structures made of brittle materials would have different fracture values depending on their sizes. They calculated the R-curve for the studied cases by using the size-effect law obtained by fitting the peak load achieved for each specimen size against the specimen width. In addition they used finite elements simulations to calculate the geometric correction factor for double edge specimens in order to relate K_I and G_I. Knowing the size-effect law and the G_I - K_I they were able to calculate the driving force curve for a wide range of specimens size and from the relations proposed by BAŽANT e PLANAS [35], calculate the R-curve [36–38]. A more detailed explanation on this methodology is shown in section 3.3.3

2.5 Digital Image Correlation on fracture mechanics

Introduced by SUTTON *et al.* [39] in early 80, and improved over the years, the digital image correlation has been used for researchers from different areas for the last decades and been established as a powerful and accurate method for displacements measurement. Among its advantages are:

- Contactless technique
- Non-destructive
- Full-field displacements
- Wide range of strain measurements
- Sub-pixel displacements

- Small time-scale events (high speed cameras)
- Either 2D and 3D fields
- Applies from small specimens to large structures

On the other hand, the method require some attention on the analysed area preparation and the image acquisition system [40].

This section presents a review of papers on digital image correlation technique relevant to this work, besides those cited in section 3.3. It includes papers that does not match the full scope of the thesis but bring pertinent conclusions about the technique in the context of fracture mechanics.

ROUX *et al.* [41] published an explanatory review on DIC technique, emphasised some aspects of the technique which endorse its use on fracture studies. According to them, the digital image correlation can act as a link between model and experiment and it is beneficial from uncertainties and noise reduction perspective to be aligned with analytical or numerical modelling. They also emphasises the importance of the technique in cases of very thin cracks, making it possible the quantification of fracture parameters.

KIRUGULIGE *et al.* [42] conducted mode-I in edge cracked epoxy samples, in a TPB configuration, dynamically loaded by an impactor, at $4.5ms/$. Images were captured at a frame rate of 225,000 fps and then processed by DIC. Crack opening displacement (COD) field was then used for stress intensity factor calculation, based on the asymptotic expressions for both dynamically loaded stationary and steadily moving cracks. They calculated both stress intensity factor and T stress from full-field displacements measurements and found a very good agreement with finite elements analysis results, concluding that DIC is a powerful method on assessment of fracture in real time.

CATALANOTTI *et al.* [43] proposed a methodology for obtaining the crack resistance curves of IM7-8552 material by digital image correlation. The technique was applied to both compact tension (CT) and compact compression (CC) specimens and intended to overcome difficulties previously encountered on solutions involving finite elements analysis such as the presence of kink-bands and the need for optical determination of the crack tip. They implemented an algorithm to automatically identify the crack tip location based in the displacement fields that considers the displacement field discontinuity due to the presence of a crack. The R-curve is then obtained by calculating the J-integral over a closed contour on the crack tip vicinity and assign the respective crack increment Δa. They reported great agreement between DIC and FEM results a for CT experiments, suggesting DIC as a valid approach, while for the CC, they said the use of DIC is an improvement over FEM technique because the later overpredicts the fracture toughness due to inaccurate numerical results.

BECKER *et al.* [44] combined finite elements method and digital image correlation for fracture toughness calculation. Their proposal consisted in carry a finite elements analysis of the displacement fields obtained by digital image correlation, by applying the strain-displacements relation to calculate the strain fields, and consequently, the stress components. From the stress fields, J-integral was calculated

17

over the area domain. They applied their technique to different loading conditions and concluded that the method is satisfatory for both quasi-brittle and elastoplastic materials.

Similarly to LEE *et al.* [21], HOU e HONG [45] used analytical displacement fields to fit experimental results obtained from DIC to calculate the R-curve of cross-ply laminate. Additionally, they also calculated the R-curve by energy integrals, in a similar way to CATALANOTTI *et al.* [43], over far field stresses obtained from gradients calculated by numerical differentiation of displacement fields, from DIC results. They reported a good agreement between the implemented methods.

GAO *et al.* [46] studied the load rate sensitivity in the fracture propagation of rocks by using digital image correlation. The specimens were dynamically loaded by a SHPB in a notched semi-circular bend (NSCB) geometry, similar do a three-point bend test. Their study relies on the same data reduction strategy cited above, by non linear least squares regression of displacements fields obtained by DIC into analytical asymptotic expressions of the displacements where teh unknowns are the stress intensity factors and the crack location.

ALLAER *et al.* [47] tested ductile epoxy specimens under quasi-static bending for fracture toughness determination. They followed the same strategy as CATA-LANOTTI *et al.* [43], HOU e HONG [45] by calculating the J-integral direct from full-field measurements obtained by DIC. In parallel they calculated the fracture toughness in two other different ways: by finite elements simulation and by ASTM standard analytical solutions. They found great agreement between the DIC results, finite elements simulations, and the analytical results concluding that the direct calculation from DIC full-fields are suitable for fracture toughness calculation.

Chapter 3

Methodology

The following sections intend to explain, in details, the whole procedure undertaken to obtain the energy release rates from the initial steps of specimen preparation and SHPB tests, to image processing and area domain integral calculations.

3.1 Experimental tests

The experimental work described in this thesis was performed by the Chair of Carbon Composites team at Faculty of Mechanical Engineering, Technical University of Munich, as part of a joint research including the Departments of Mechanical Engineering of the Faculty of Engineering of the University of Porto and the Metallurgical and Materials Engineering Program of Federal University of Rio de Janeiro. Two data reduction strategies have been followed to analyse the experimental data (figure 3.1): the first, published by KUHN *et al.* [16], relies on the size effect-law allied to finite elements simulations to determine the dynamic R-Curve of the material; the second methodology, presented in this thesis, used the full-field measurements obtained by DIC to calculate the dynamic J-Integral over the loading history and determine the dynamic energy release rate at the fracture initiation. For the purpose of the joint research the same set of experimental data was use by both analysis strategies.

3.1.1 Material and tests specimens

Material

The material analysed in the present work is the HexPly®8552 Unidirectional Carbon Prepregs (with IM7 carbon fibres) by Hexcel. It is a hot cure matrix system with nominal thickness of $0.131mm$ and 57.70% fibre volume per cured ply. This material has been previously used in past studies from the research group [16, 17, 36–38, 43, 48, 49]. The prepreg mechanical properties are shown in table 3.1.
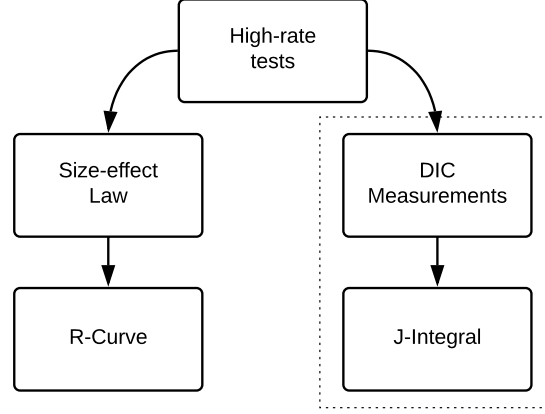
Figure 3.1: Data reduction strategies. The dotted line shows the approach followed in this thesis.

Table 3.1: Mechanical properties of HexPly®8552-IM7 at $25°C$

$E_1(GPa)$	$E_2(GPa)$	$X_T(MPa)$	$Y_T(MPa)$
164	12	2724	64

Specimens

The specimen geometry chosen was the double edge notched (DENC[1] - figure x), previously used by the group in quasi-static fracture analysis [36, 37]. Flat panels were manufactured in a $[90°/0°]_{8S}$ layup configuration resulting in $4mm$ thick (32 plies), balanced laminates. The panels were cured by hot-pressing following the manufacturer guidelines [50] and then machined into DENC geometry. The preparation process is also described by KUHN *et al.* [16]. Table 3.2[2] shows quasi-static (QS) and high-rate (HR, $\dot{\epsilon} = 100s^{-1}$) elastic properties of the laminate.
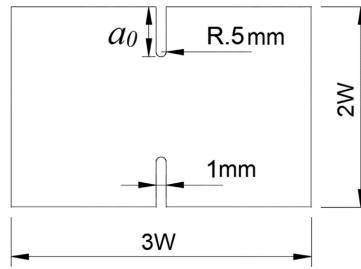
Figure 3.2: Double edge notched specimen geometry.

As mentioned, the same experimental data would be used by both research branches, shown in figure 3.1. Therefore, the specimens were cut in four different sizes (referred here as *Types* - the specimen nomenclature follows type.number, *e.x. III.2* stands for specimen #2 of type III), keeping the same dimensional ratio.

---

[1]C denotes compressive tests

[2]Properties found in KUHN *et al.* [16]

Table 3.2: Elastic proerties of the laminate.

	$E_x = E_y(GPa)$	$G_{xy}(GPa)$	ν_{xy}
QS	67.449	5.068	0.042
HR	67.126	6.345	0.048

Table 3.3: Specimens dimensions

	$a_0(mm)$	$2W(mm)$
Type I	2.50	10
Type II	3.75	15
Type III	5.00	20
Type IV	6.25	25

It follows the size-effect law approach used by CATALANOTTI *et al.* [36, 37] and further by KUHN *et al.* [16] (left-hand side branch). This strategy will be further discussed in section 3.3.3. Dimensions are shown in table 3.3.

The specimens surface were then covered by a random black and white speckle for further DIC analysis and post processing, as shown in figure 3.3.

(a) Illustration of a specimen surface.

(b) Type II specimen with applied speckle.

Figure 3.3: Random speckle applied to a specimen.

3.1.2 Experimental setup and high strain rate tests

The experimental procedure was carried out in a split-Hopkinson pressure bar (SHPB), with a classic configuration (striker, incident, and transmitted), shown in figure 3.4. Previous analysis had been done to define the proper bar diameter, pulse shaper thickness, and striker velocity to guarantee specimens of different types would be under the same strain rate condition ($\dot{\epsilon} = 100s^{-1}$). The striker velocity varied from 8.6 to $12.2m/s$ in respect of specimen size. For each specimen the peak load was recorded for further use in data reduction strategy.

For full-field measurements, each specimen surface (figure 3.3b) was recorded during the whole loading history. The images were acquired at 300,000 frames per second ($3.33\mu s$ intervals), enabling the assessment of the stress fields at fracture events time scale. The equipment used was a PHOTRON camera, model AS-Z,
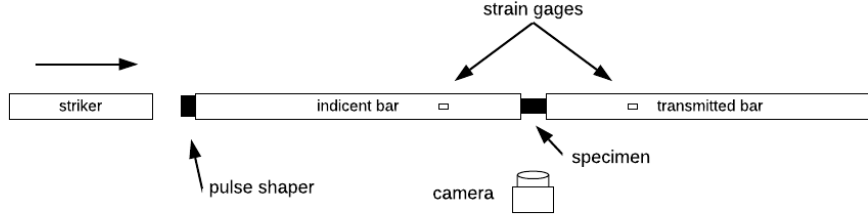
Figure 3.4: SHPB setup.

with spacial resolution set to 256 x 128 px^2 in grey scale (intensity channel only)[3]. A detailed description of the experimental setup is found in KUHN *et al.* [16].

3.2   Post processing

The post processing is the initial part of the methodology proposed in this thesis. It intends to calculate precise full-fields from image frames acquired during the high-rate tests to be further used in data reduction. As indicated in figure 3.5, user defined parameters are needed as part of calculations, this section proposes a framework to be followed for strain fields and time derivative fields calculations.
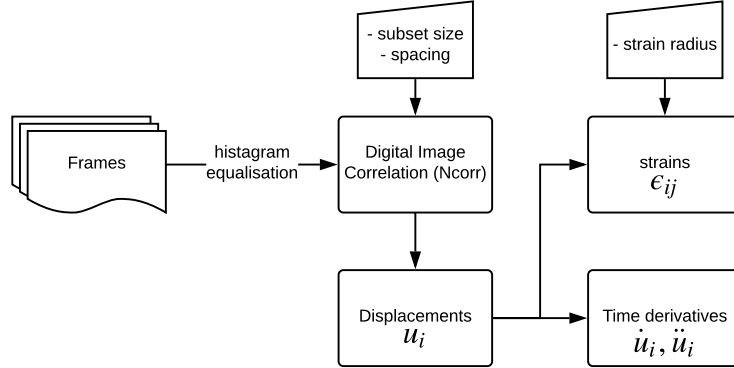
Figure 3.5: Images post processing flowchart.

3.2.1   DIC parameters estimate

Subset radius model

The primary objective of the digital image correlation, in solid mechanics context, is to find a mapping function that relates a subset from in original image to its correspondent in the deformed configuration image. By finding a subset in the

---

[3]Except for *II.1* that was recorded in 128 x 120 px^2 at 400,000 fps

deformed image, which paired to a subset in the original image, optimises a given correlation function.

Different functions can be used as the objective function. Ncorr uses two different correlation criteria, cross-correlation criterion and least-squares correlation criterion. The cross correlation is used to find initial guesses for the non-linear optimisation of the least-squares criteria, that uses a local minimisation method (Gauss-Newton) [1]. Unique subsets are desirable for proper determination of displacement fields, otherwise it would result in multiple local minima with close values leading to a ill-posed problem, highly sensitive to the initial conditions. For this purpose, specimens without a high contrast, random surface texture, such as in the present work, should be therefore covered by such, as previously explained in section 3.1.

Figure 3.6: Subset size model

The strategy adopted in this thesis takes into account the size and distribution of the speckle particles resulting in a heuristically determined geometric model following the recommendation of the number of particles within a subset found in [51]. Some considerations have been made on model development:

i At least three speckles per subset [51]

ii Speckles are considered perfectly circular

iii Particles are distributed at the vertexes of equilateral triangles.

iv The speckle size covers 95% of particles sizes, in this case the Feret diameter.

v The near neighbour distance is the distance that covers 95% of the free mean path distribution.

The resulting geometric model is shown in figure 3.6. For determining the value of the subset radius, the equation 3.1 is used.

$$SR = D_{95} + NND_{95}\frac{\sqrt{3}}{3} \tag{3.1}$$

The feret diameter and the free path distributions of speckekles were obtained by image processing techniques, illustrated in figure 3.8, by using the open source software ImageJ, as follows:

(a) Illustration of a specimen surface.

(b) Type II specimen with applied speckle.

(c) Illustration of a specimen surface.

(d) Type II specimen with applied speckle.

Figure 3.7: Random speckle applied to a specimen.

Image processing

Prior to the speckle particles analysis, an image processing step was done. It comprises four intermediate steps performed in the software ImageJ [52], listed as follows:

i Histogram equalisation: This operation intends to enhance contrast for further threshold classification. It remaps the intensity histogram to the full spectrum of intensity levels To enhance the contrast by stretching out the intensity distribution to the whole range of intensity spectrum (Figure 3.7).

ii Classification: Image binarisation by Bernsen adaptive threshold filter [53], with a $15 \times 15px^2$ window. Pixels with lower intensity values, or darker regions, are classified as particles, while higher intensity values relate to the background. (Figure 3.8c).

iii Watershed: this transformation aims to separate touching objects avoiding overestimating particles size (Figure 3.8d).

iv Area filter and despeckle: Removes particles smaller than $4px^2$ and smooth sharp regions of objects as a fine tuning step for more accurate calculation of distances between centres (Figure 3.8d).

Subset spacing

The subset spacing parameter defines the gap, in pixels, between two consecutive subsets. That is, if this parameter is null, for each pixel of the image, the subset of its
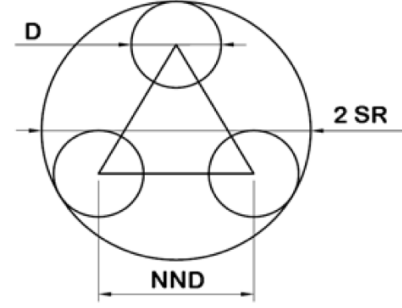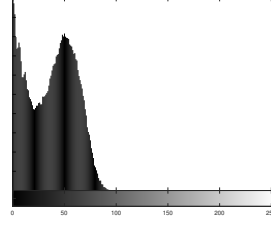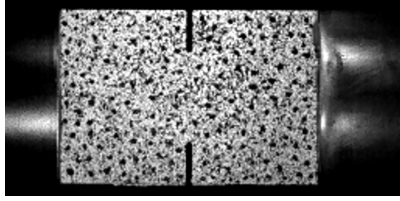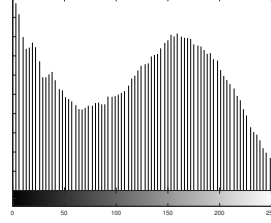
24

(a) Illustration of a specimen surface.　　(b) Type II specimen with applied speckle.

(c) Illustration of a specimen surface.　　(d) Type II specimen with applied speckle.
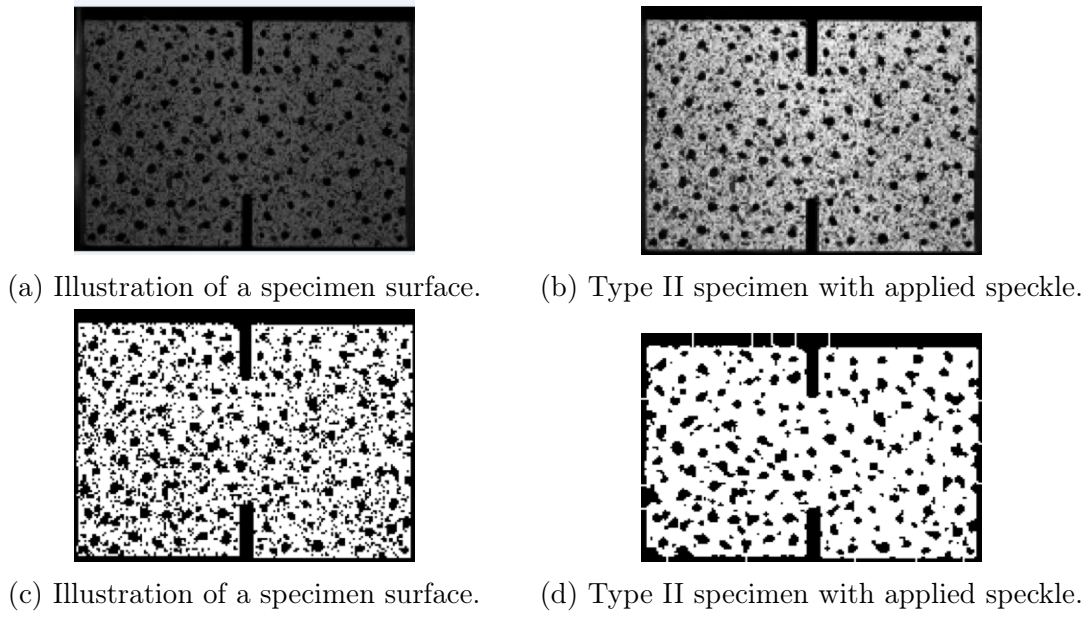
Figure 3.8: Random speckle applied to a specimen.

vicinity will be included to analysis. The idea behind this parameter is to minimise the computational effort in case of high resolution images. Images present in this work compromises spatial to time resolution, resulting in low resolution images. The main objective of this study is area integral calculations. For such low resolution the performance *vs.* accuracy trade-off does not apply. Therefore, the spacing was set to null for all frames and the maximum number of data-points were acquired, meaning that the full-fields have the same resolution as the input images. Image 3.9 shows examples of displacement fields for subset spacing of 0, and $5px$.

(a) Spacing = 5　　　　　　　　　　(b) Spacing = 0
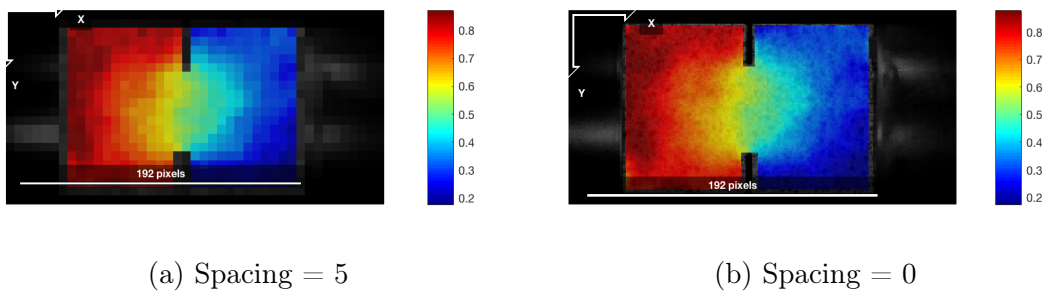
Figure 3.9: u displacement field.

3.2.2　Region of interest

Additionally, Ncorr uses the concept of *region of interest* (ROI). I is a boolean mask that defines the valid domain for the digital image correlation. It means that only full-field displacements and strains will only be computed for pixels matching *True* in their respective mask (white pixels on figure 3.10).

25
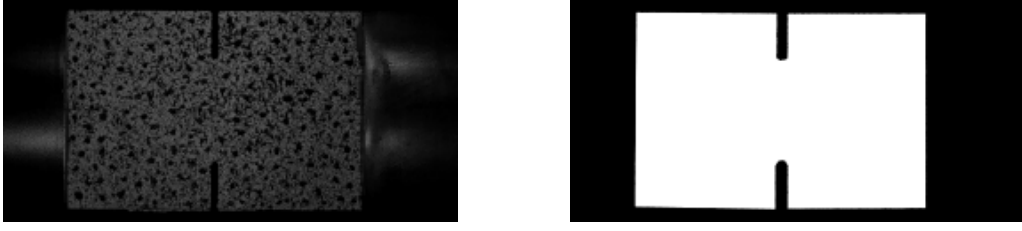
Figure 3.10: Specimen and its respective ROI.

3.2.3 Strain computing

Ncorr uses Green-Lagrange strain tensor (Equation 3.2) on its implementation, high order displacements derivatives can be neglected for the present case, therefore the small deformations framework was used. Four derivatives are needed, assuming a bi-dimensional case.

$$\epsilon_{ij} = \frac{1}{2} \left(\frac{\partial u_i}{\partial x_j} + \frac{\partial u_j}{\partial x_i} + \frac{\partial^2 u_k}{\partial x_i \partial x_j} \right) \tag{3.2}$$

In the correlation step, the generalised deformation vector, $p = \{u_1, u_2, \frac{\partial u_1}{\partial x_1}, \frac{\partial u_2}{\partial x_2}, \frac{\partial u_2}{\partial x_1}, \frac{\partial u_2}{\partial x_2}\}^T$, is obtained. It contains the derivatives for computing the strain tensor, but as mentioned by authors, the displacement gradient obtained is noisy and should go through some smoothing process. Instead, Ncorr uses the concept of strain window. It consists in finding the plane that best fits the data within a defined "window", by solving the equation 3.3 for all n data points within each window. Then, the displacement gradients are used in equation 3.2.

$$\begin{Bmatrix} u_{1,0} \\ \vdots \\ u_{1,n} \end{Bmatrix} = \begin{bmatrix} 1 & x_{1,0} & x_{2,i} \\ \vdots & \vdots & \vdots \\ 1 & x_{1,n} & x_{2,n} \end{bmatrix} \begin{Bmatrix} a_i \\ \frac{\partial u_1}{\partial x_1} \\ \frac{\partial u_1}{\partial x_2} \end{Bmatrix} \tag{3.3}$$

Larger strain window would oversmooth and homogenise the full-field strains, reducing accuracy in areas that would present strain concentration, such as crack and notches vicinity, so there is a trade-off between accuracy and proper localisation description [47]. Strain window analysis is included as part of parameters analysis and its influence on obtained J-Integral value is further discussed.

3.2.4 Time derivatives

Besides the spatial gradients, the data reduction strategy includes the second time derivative on its formulation, i.e. acceleration fields. The extended area integral

26

computed in this thesis (Section 3.3) includes the inertial term for its formulation and therefore the the acceleration components are needed to properly compute its contribution to the total energy involved. In the present methodology the time derivatives are computed by using the Savitzky-Golay filter. It consists in a moving polynomial fit, of order p and data set size Δh, over the data series replacing the data point value by its corresponded fitted value, the result is smoother series as illustrated in figure 3.11. The idea behind the filtering in the present work is not primarily smoothing, but calculating the derivatives. Instead of using finite differences, the nth derivative are computed by polynomial differentiation, using the polynomial coefficients as in equation 3.5, obtained by polynomial regression.
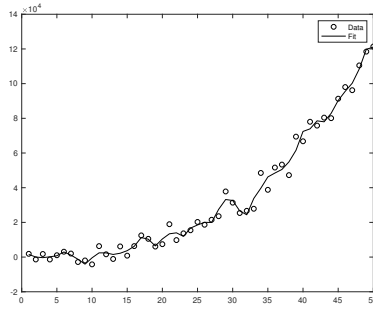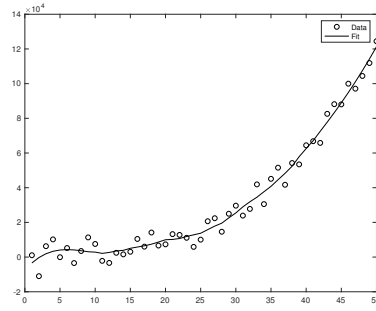
(a) $\Delta h = 5$ data points. (b) $\Delta h = 17$ data points.

Figure 3.11: Third order Savitzky-Golay filter applied to $f(x) = x^3 +$ random noise.

$$P(x) = \sum_{i=0}^{p} C_i x^i \tag{3.4}$$

$$P^n(x) = \sum_{i=n}^{p} \frac{i!}{(i-p)!} C_i x^{(p-i)} \tag{3.5}$$

3.3 Data reduction

The present methodology carries a data reduction strategy based on full-field measurements. A generalised J-Integral, is calculated around the notches ([54, 55]). Energy integrals alongside full-field measurements have been proven to be a suitable way to quantify fracture parameters. In section 2, several cited authors make use of J-integral in their fracture quantification approaches but the lack of literature for the application to the case studied in this thesis, that is, the high rate compressive fracture of fibre composites, is a motivation to investigate the suitability of this novel approach. For integral calculations, discussed in section 3.3.1, the following full-fields were required: the stress components, the displacements gradient, and the acceleration components. The later is used to calculate the contribution of inertia

to the fracture process and verify if the quasi-static approach is suitable for proper phenomenon description. The strategy adopted to calculate the energy integrals from recorded test images are illustrated on figure 3.12.
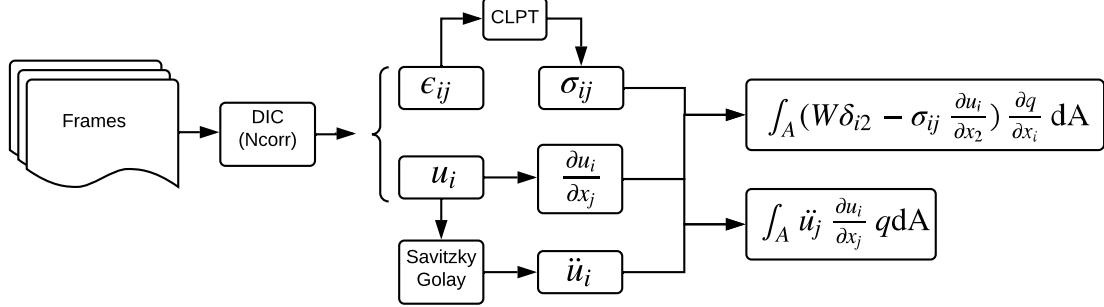
Figure 3.12: Flow diagram for area domain integrals from experiment images

3.3.1 Dynamic energy release rate derivation

Formulation

The generalised J-integral for dynamic events includes in its formulation the contribution of the kinetic energy and the inertia. Compared to the classic "static" J-integral, it contains additional terms for velocity and acceleration fields [54, 55]. Following equations show briefly the steps found in KUNA [55] to derive the the most general J-integral for dynamic processes with additional terms in bold from energy fluxes $\dot{w}_c$, adding the kinetic energy T to the energy balance (Equation 3.6). Considering the linear elastic fracture mechanics where the J-integral corresponds to the energy release rate G:

$$\dot{w}_c = \dot{w}_{internal} - \dot{w}_{external} - \dot{T}$$
$$G^{dyn} = \frac{\mathrm{d}w_c}{\mathrm{d}a} = \frac{1}{\dot{a}}(\dot{w}_{internal} - \dot{w}_{external} - \dot{T})$$

gives

$$G^{dyn} = \frac{1}{\dot{a}} \left[\int_{\Gamma} t_i \dot{u}_i \mathrm{d}s - \frac{d}{dt} \int_A \left(U + \frac{\rho}{2} \dot{u}_i \dot{u}_i \right) \mathrm{d}A \right]$$

Considering a moving coordinate system (moving crack), applying the Reynold's transport theorem to the time derivative yields to

$$\frac{d}{dt} \int_A \left(U + \frac{\rho}{2} \dot{u}_i \dot{u}_i \right) \mathrm{d}A = \int_A \left(\frac{\partial U}{\partial t} + \rho \dot{u}_i \ddot{u}_i \right) \mathrm{d}A - \dot{a} \int_{\Gamma} \left(U + \frac{\rho}{2} \dot{u}_i \dot{u}_i \right) n_1 \mathrm{d}s$$

Substituting the dynamic equilibrium $\text{div}\sigma = \rho\ddot{u}$ and the strain-displacement relation for U (considering $T = \frac{\rho}{2}\dot{u}_i\dot{u}_i$), and applying the Gauss' theorem

$$G^{dyn} = \int_\Gamma \left((U + \boldsymbol{T})\delta_{1j} - \sigma_{ij}\frac{\partial u_i}{\partial x_1} \right) n_j \, \mathrm{d}s + \int_{\boldsymbol{A}} \left(\rho\ddot{\boldsymbol{u}}_{\boldsymbol{i}}\frac{\partial \boldsymbol{u_i}}{\partial \boldsymbol{x_k}} - \rho\dot{\boldsymbol{u}}_{\boldsymbol{i}}\frac{\partial \dot{\boldsymbol{u}}_{\boldsymbol{i}}}{\partial \boldsymbol{x_k}} \right) \, \mathrm{d}\boldsymbol{A} \quad (3.6)$$

for a stationary crack ($\dot{a} = 0$), equation 3.6 can be simplified to

$$G^{dyn} = \int_\Gamma \left(U\delta_{1j} - \sigma_{ij}\frac{\partial u_i}{\partial x_1} \right) n_j \mathrm{d}s + \int_A \rho\ddot{u}_i\frac{\partial u_i}{\partial x_1}\mathrm{d}A \quad (3.7)$$

WU e DZENIS [7] mentioned that the use of area integrals is improper for energy calculations near crack tips because it includes the singularity point. This proposition does not apply for the present case because the energy release rate is calculated for a point in the loading history immediately before the fracture initiation. Before this point the stress fields there is no singularity, because there is no crack tip yet, only the notches.

In addition, the domain transformation requires the use of the weight function q, that should match the following criteria:

i Must smoothly vary from 0 (at the outer contour) to 1 (at the inner contour);

ii Must value 1 within the inner contour γ_i;

iii Must remain 0 out of the out contour.

Weight function

A bi-quadratic function (Equation 3.8), was chosen. It matches the above criteria and plays an important role in the practical calculation because it defines the integration boundaries, and weights the contribution of each data-point to the total energy release rate value. The domain boundaries are controlled by the parameters c and h (*i.e.* domain width and height). For the quasi-static term, only its derivative is taken, as in equation 3.7. By changing the parameters it is possible to neglect the singularity point by matching the third criteria, where the derivative would remain zero, as shown in figure 3.13[4].

$$q(x, y) = \gamma_i \left(\frac{c^2 - x^2}{c^2} \right) \left(\frac{h^2 - y^2}{h^2} \right) \quad (3.8)$$

---

[4]derivatives are rotated in 180° to facilitate visualisation.
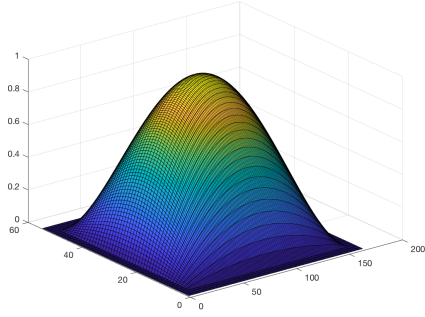
(a) $q(x_1, x_2)$, $\gamma_i = 0$.
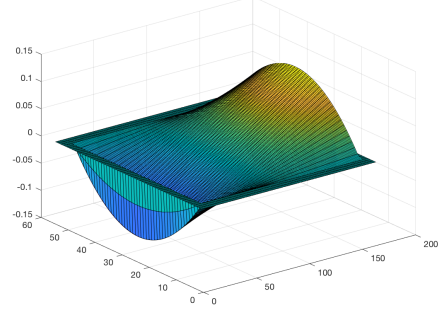
(b) $\frac{\partial q}{\partial x_1}$.
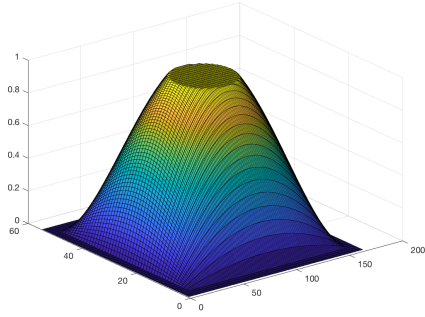
(c) $q(x_1, x_2)$, $\gamma_i = 0.075$.
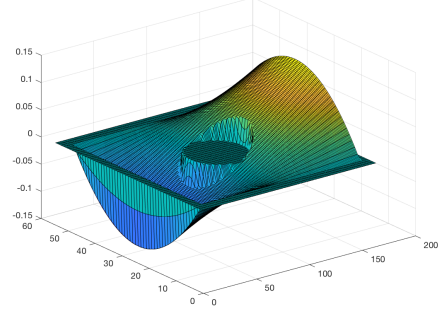
(d) $\frac{\partial q}{\partial x_1}$.

Figure 3.13: Weight function q.
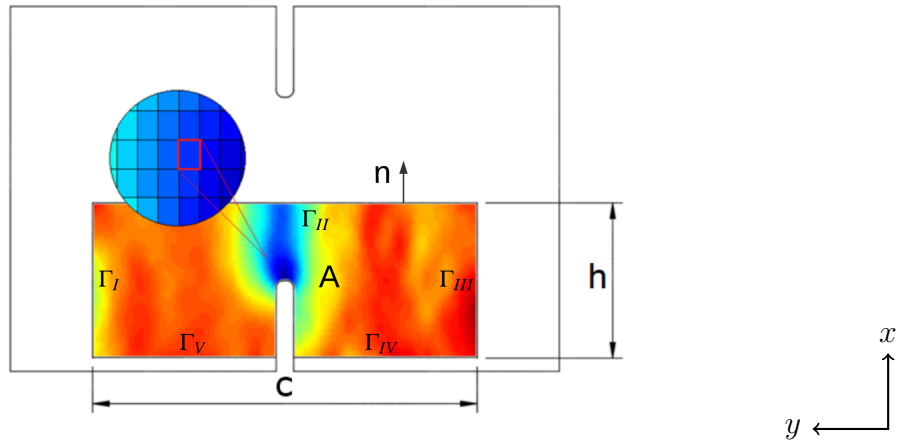
Figure 3.14: Integration domain for bottom notch illustrated by σ_{xx} and a data-point in the notch vicinity.

Stress fields calculation

From full-field strains, the stress fields are calculated by applying the constitutive relation for the material (Equation 3.9[5]). The material stiffness matrix $[C]$ is calculated for the stacking sequence referred in section 3.1 applying the classical laminated plate theory (CLPT) to data from table 3.2.

$$\{\sigma'\} = [C]\{\epsilon'\} \tag{3.9}$$

Discrete implementation

The energy release rate is calculated by a discrete implementation of equation 3.6. It sums the contribution of each one of the data points (dp) in the area domain to the J-integral value, including the inertial term (Equation 3.10). The spatial gradients are calculated by $\Delta u_i/\Delta x_j$, corrected to proper spatial conversion ($\Delta x_1 = \Delta x_2 = \text{spacing} \times mm/px$). Similarly, for the contour domain (Γ) integration, the contribution of each data point on the domain boundaries are summed. The contour domain is defined by the four edges that bounds the area domain ($\Gamma = \Gamma_I + \Gamma_{II} + \Gamma_{III} + \Gamma_{IV}$) and their respective normal vectors, pointing outwards, are $n_I = (-1, 0), n_{II} = (0, -1), n_{III} = (1, 0)$, and $n_{IV} = (0, 1)$.

$$\tilde{G}_A = \sum_{dp} \left[\left(W\delta_{2i} - \sigma_{i2}\frac{\Delta u_i}{\Delta x_2} \right) \frac{\Delta q}{\Delta x_j} \, \mathrm{d}s + \rho\ddot{u}_i\frac{\Delta u_i}{\Delta x_j}q \right]_{dp} \Delta x_1\Delta x_2 \tag{3.10}$$

$$\tilde{G}_\Gamma = \sum_{\Gamma=I}^{V} \sum_{dp} \left(W\delta_{2i} - \sigma_{i2}\frac{\Delta u_i}{\Delta x_2} \right) n_2 \, \mathrm{d}s + \sum_{dp} \left(\rho\ddot{u}_i\frac{\Delta u_i}{\Delta x_j}q \right)_{dp} \Delta x_1\Delta x_2 \tag{3.11}$$

The integration domain is controlled by the weight function q and its spatial derivatives, which is set to null for dp outside the boundaries. The domain is centred in the mid-point of the arc formed by the notch and its boundaries are set by the parameters c and h (domain width and height, respectively). One may notice that, as in figure 3.14 only one of the notches has its domain represented.

In the proposed methodology the energy release rate is calculated individually for each notch n (here defined as *top* and *bottom*), considering independent stress fields for each of them. The process repeats for every frame f and $\tilde{G}_n(f)$ is stored for each notch as a time series, as shown in algorithm 1.

---

[5]prime symbol indicates global coordinates

Algorithm 1 $\tilde{G}_n(f)$ calculation.

1: **for each** $f \in$ Images **do**
2:     $u_i(f) \leftarrow \text{DIC}(f)$
3:     $\epsilon_{ij}(f) \leftarrow \text{DIC}(f)$
4:     $\sigma \leftarrow C\epsilon$
5:     $\ddot{u} \leftarrow \text{SGolay}(u)$
6: **end for**
7: **for each** $n \in$ Notches **do**
8:     **for each** $f \in$ Images **do**
9:         $\tilde{G}_n(f) \leftarrow \sum_{dp}(W\delta - \sigma\nabla u\nabla q + \rho\ddot{u}\nabla uq)\Delta x\Delta x$
10:     **end for**
11: **end for**

Dynamic fracture toughness definition

The initiation fracture toughness G_{IC} is defined as the point of instability. In the present work, the driving force for each specimen type, at constant load regime, is calculated for the peak-load σ_u achieved during the experimental test, following KUHN *et al.* [16], BAŽANT e PLANAS [35]. The energy release rate history was captured for each specimen and the fracture initiation frame f_p is defined as the peak-load frame, corresponding to the instant of the peak-load measured during the tests.

The fracture toughness calculation consisted in a polynomial fit of the $\tilde{G}(f)$ values over time for each specimen, following the process bellow:

 i First a time window was selected. Previous analyses show that 23 frames are enough to comprise all the relevant process. It means that the fracture initiation, from an unloaded state occurs within $\Delta t = 230\mu s$;

 iv A third order polynomial was used to fit $\tilde{G}(f)$ and the value of the fitted curve at f_p is assumed to be the fracture initiation frame.

 v The process is done for both notches and the higher value is taken as G_{IC}. The choice for the higher value is based on the assumption that at the peak load, the first crack propagates from the notch under the higher stress intensity factor condition.

So the calculated $G_{IC} = \tilde{G}(f_p)$, corresponding to the initiation frame, represents the point of $G(\Delta a)$ curve which the fracture process looses stability, that is, $G_I \geq R$, as shown in figure 3.15
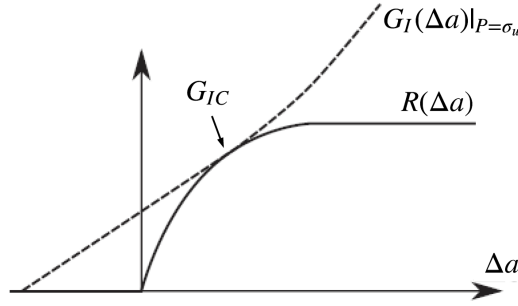
Figure 3.15: Driving force at constant load and R-curve.

3.3.2 Parameters sensitiveness analysis

In the proposed methodology four independent parameters are used in the analysis. In the digital image correlation step, the subset size is deterministically calculated based on the image speckle applied to the specimen surface. Despite being part of the DIC step, the strain window is analysed alongside the domain dimensions (width and height), and the inner contour size. These parameters do not rely on physical characteristics of the specimen itself, but on calculated full-fields, therefore a phenomenological approach applies.

Full factorial design

The full factorial design was chosen to assess de influence of the parameters on calculated G_{IC}. The strain window, as previously explained in section 3.2.3 relates to the sensitivity to the smoothness of the strain field. While the domain variation verifies whether G_{IC} is dependent to the integration domain. The presence of the inner contour (γ_i) excludes the contribution of the crack tip vicinity data points, avoiding miscalculation due to a possible singularity, when applicable. Five levels were heuristically chosen for each one of the four independent parameters, resulting in 5^3 runs. Table 3.4 shows the chosen levels for each parameter.

Table 3.4: Full factorial design.

Parameter	Level 1	Level 2	Level 3	Level 4	Level 5
Strain window (SW)	5	7	9	11	13
Domain width (c)	50%	60%	70%	80%	90%
Domain height (h)	50%	60%	70%	80%	90%
Inner contour (γ_i)	0.00	0.02	0.04	0.06	0.08

Parameters influence

Three scenarios were tested for assessing the influence of the parameters on the G_{IC} value.

    i 4 parameters variation: the full factorial design

    ii 3 parameters variation: inner contour fixed at $f = 0.00$ and a full factorial for the other three parameters;

   iii 2 parameters variation: strain window fixed at a value of 9 data points, and the domain parameters varying from 50% to 90% of the specimen size in the respective direction;

   iv 1 parameter variation: strain window fixed at a value of 9 data points, the domain width fixed at 90% of specimen width, varying the domain height from 50% to 90% of the specimen half height.

Then for each the above scenario the coefficient of variation $\%Var$ is taken as the variability measurement, calculated as follows, dividing the standard deviation by the average value.

$$\%Var = \frac{SD_{G_{IC}}}{\mu_{G_{IC}}} \tag{3.12}$$

Note the for the two last scenarios, the coefficient of variation also a measurement of the path independence, assessing whether or not the energy flux forms a conservative field.

Parameters relative importance

Besides the investigation of the individual and combined parameters influence in the calculated value of G_{IC}, it was also performed the analysis of the relative influence (RI), that is, how much the parameter contributes to the dependent parameter.

Previous Lilliefors' analyses have shown that the residuals do not fit properly in a normal distribution. It means that the effects analysis using the ANOVA table does not suit to the present study. The quantification of the contribution each input parameter has on G_{IC} was achieved by training an artificial neural network (ANN) and then looking into its resulting weights. A multilayer perceptron (MLP) ANN with five hidden neurons within a single hidden layer (Figure 3.16) was heuristically chosen. The parameters importance were assessed by using the *Connection Weights Method* (CWM).
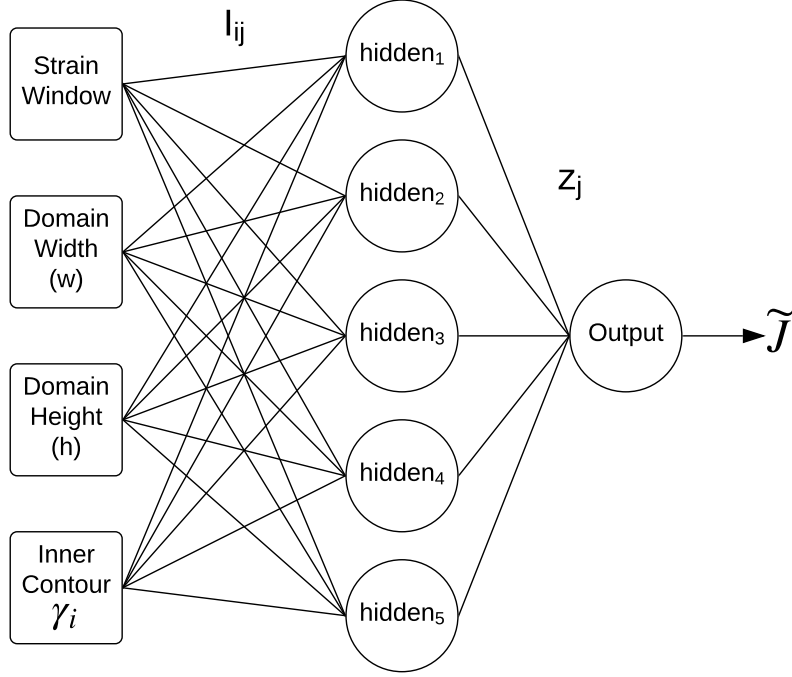
Figure 3.16: ANN with one neuron.

The CWM had been successfully used to estimate RI for each parameter based on the weights of a trained ANNs [56]. The relative influence, or importance, of a given input parameter can be defined by equations 3.13 and 3.14, for the case of a single hidden layer.

$$RI_i = \sum_{j}^{N_h} I_{ij} Z_j \tag{3.13}$$

$$RI_{i\%} = \frac{RI_k}{\sum_k RI_k} \tag{3.14}$$

where N_h is the total number of hidden nodes, I_{ij} is the weight of the connections between the ith input node and the jth hidden node, and Z_j is the weight of the connection between the jth hidden node and the output node.

3.3.3 Comparison with the R-Curve

KUHN *et al.* [16] suggest the existence of a rising R-curve for the studied material. The assumption of the R-curve is tested in the present thesis, following the strategy proposed and used in previous works [36–38, 43], by using the size-effect law determined in the experimental procedure, aiming to establish a relation between the specimen size and the instability point (*i.e.* the crack increment that represents

the point of instability). The following derivation, found in KUHN *et al.* [16], was used to calculate the instability point (Δa_c) for each specimen type, resulting in $\{w, \Delta a_c\}$ data points, and consequently $\{G, \Delta a_c\}$.

Mathematical model

BAŽANT e PLANAS [35] propose that for cases where the driving force $G(\Delta a)$ increases with the crack increment, it intercepts the resistance curve $R(\Delta a)$ at the point of instability (Δa_c). The same applies for its derivative, leading to the system described by equation 3.15.

$$\begin{cases} G(\Delta a_c) & = R(\Delta a_c) \\ \frac{\partial G(\Delta a_c)}{\partial \Delta a} & = \frac{\partial R(\Delta a_c)}{\partial \Delta a} \end{cases} \tag{3.15}$$

First, from the relation between G_I and K_I

$$G_I = \frac{1}{E}\sqrt{\frac{1+\rho}{2}}K_I^2 \tag{3.16}$$

Writing K_I in terms of the far field stress:

$$K_I^2 = \phi \sigma^2 W \tag{3.17}$$

In the present case, the correction factor $\phi = \phi(\alpha)$, where $\alpha = (a_0 + \Delta a)/W = \alpha_0 + \Delta a/W$. Combining equations 3.16 and 3.17, using $\xi = \frac{1}{E}\sqrt{\frac{1+\rho}{2}}$, yields to

$$G_I = \xi \phi \sigma^2 W \tag{3.18}$$

Considering that the R-curve is an intrinsic property of the material for given a strain rate, not geometry dependent, it is correct to define that $\partial G_I/\partial W = 0$. Applying to equation 3.18,

$$\frac{\partial}{\partial W}(\phi \sigma^2 W) = 0 \tag{3.19}$$

Since ϕ and σ^6 can be expressed in terms of W, the partial derivative, in respect to W can be expressed by the fundamental theorem of calculus:

$$f(W) = \phi\left(a_0 + \frac{\Delta a}{W}\right)\sigma^2(W)W \tag{3.20}$$

$$\lim_{\Delta W \to 0} \frac{|f(W + \Delta W) - f(W)|}{\Delta W} \tag{3.21}$$

---

[6]The size-effect law $\sigma = \sigma(W)$ was extracted from KUHN *et al.* [16], it relates to the same set of tests and specimens

The value of Δa for each specimen type is so obtained by the minimising $f(\Delta a) = \partial G_I / \partial W$ subjected to $\Delta a > 0$.

For comparing the results to those obtained by KUHN *et al.* [16], the same assumption, that only the longitudinal plies contribute to laminate fracture toughness is made. Considering the studied material is a symmetrical and balanced laminate, only half of the thickness is contributing to fracture toughness, which means that the fracture toughness of the longitudinal plies $G_{IC}^0 = 2G_{IC}^{laminate}$.

Correction factor - ϕ

The correction factor ϕ for DENC specimens was extracted from a parallel work done by LONDRES [57]. He followed the same approach used by KUHN *et al.* [16] by using finite elements simulations to determine $\{G_I, \alpha\}$ value pairs to establish a relation between them. The virtue crack closure technique (VCCT) was implemented and a parametric finite elements study was performed. After the numeric simulations, a polynomial regression was used to define ϕ as a fourth order polynomial. He also presents a comparison between element types and energy calculation methods. The results pointed that quadratic elements alongside J-Integral is a good alternative for ϕ calculation.

3.3.4 Deep learning over stress fields

It had been noticed during the progress of this research that the calculation of energy release rate based on full-field stresses of dynamically loaded specimens are highly dependent on the chosen fracture initiation frame. No visual aspects aspects that would lead to a proper definition have been found, the fracture initiates several frames before the first sign of damage comes up to the specimen surface, as seen on image 3.17. As mentioned, this thesis follows the same criteria used in previous related studies, that is, the peak load during the experimental procedure ($G_{IC} = G_I(\Delta a)|_{p=p_u}$), even though the fracture process does not strictly initiate at the peak load, but more likely, at instants before [58]. Since no evidence has been found to support this hypothesis, the peak load remains as the current criterion, as suggested by [35].

This section describes a procedure to determine the probability of the crack initiation occurrence for given frame by training a convolutional neural network over the full-field stress components calculated by the DIC, using the peak load criteria as the input classification threshold.

No prior work has been found on this topic until the present date, therefore it should be seen as a conceptual approach, or a suggested research branch, rather than a methodology used for obtaining the fracture toughness.
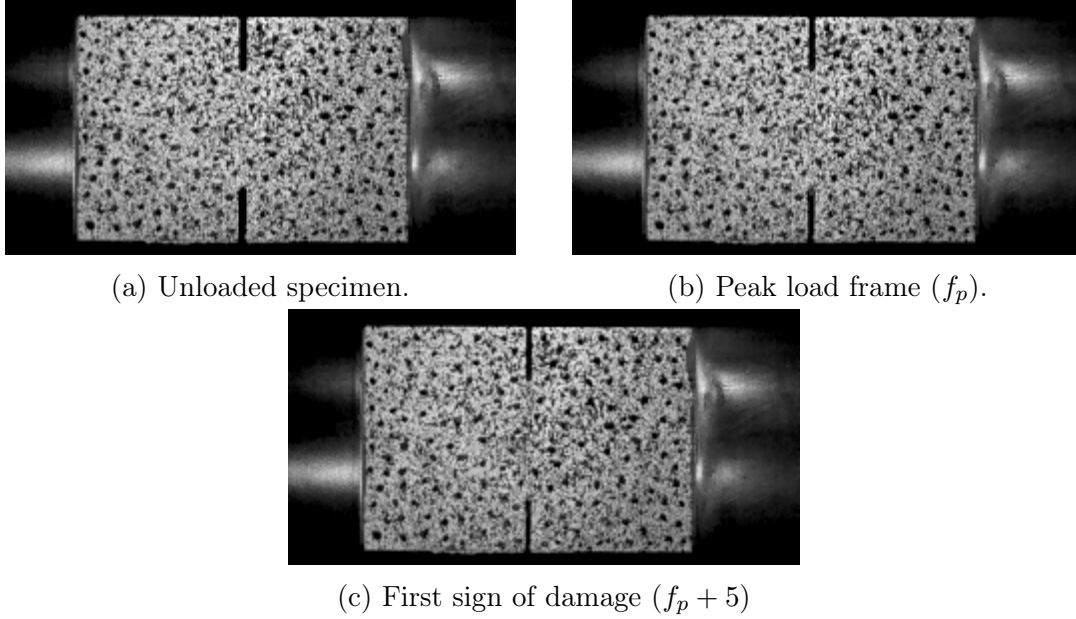
(a) Unloaded specimen.

(b) Peak load frame (f_p).

(c) First sign of damage ($f_p + 5$)

Figure 3.17: Sequence of images during the test (with adjusted histogram).

Convolutional neural networks (ConvNets)

In traditional image classifiers implemented by artificial neural networks, the pre-processing step could be highly time demanding. Prior to training, the operator should choose relevant features that could separate images into different classes then find the proper image processing filtering sequence for extracting these features. For instance, in the very simple case of classifying shapes into circles and rectangles, after extracting the objects using a filter, or kernel, like *Sobel*, the operator should calculate shape descriptors like circularity and aspect ratio to evaluate in which class the given shape would fit the best. Differently, for more complex situation, where the operator can not identify the relevant features, convolutional neural networks rise as an alternative. ConvNets became popular after *ImageNet Large Scale Visual Recognition Challenge 2010* (ILSVRC2010), when KRIZHEVSKY *et al.* [59] won the competition by using a ConvNet to classify 1.2 million images into 1000 different classes. ConvNets, in general, are composed by two major components: convolutional layers and the fully connected neural network. The first comprises a sequence of adaptive (or learnable) kernel filters for feature extraction. The more convolutional layers the ConvNet has, deeper it goes from low-level features such as edges and colours to more complex features as particular structures of each image class as a combination of lower level features. The later is the classification layer itself. It receives the output of the sequence of convolutional layers and connects it to each possible class with a probability, then the higher probability, or likelihood, is the guessed class. Figure 3.3.4 shows a basic implementation of a convolutional neural network with two convolutional layers.
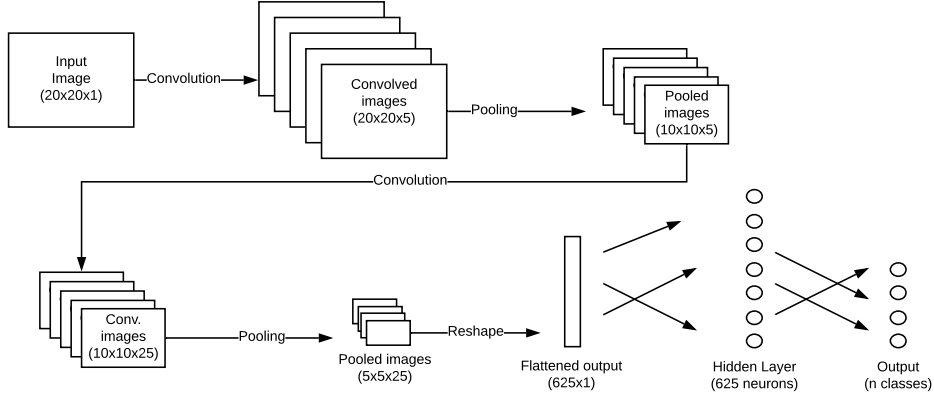
Figure 3.18: ConvNet with two convolutional layers.

The Stress "RGB" components

Originally, ConvNet image classifiers take the image channels (commonly RGB - reg, green, blue - components) as inputs and operates over them. In the present case, instead of using the intensity channel[7], the idea was to leverage the convolutional neural network through the DIC results, by using the stress components, as such. For each frame, the stress components were linearly rescaled to $0, 255$, and then combined into an image, in which the colour components are the rescaled stress fields, as in figure
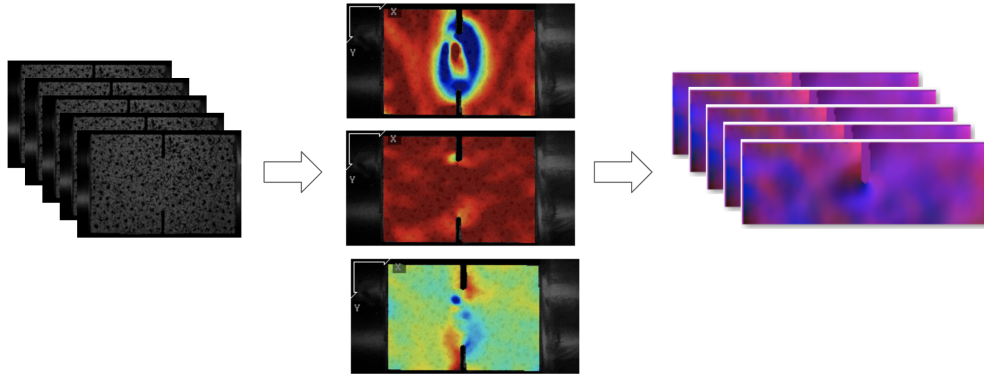
Figure 3.19: Image composed by stress components.

Training and classification

Mobilenet[60] was used for training and classification. It is a light weight ConvNet optimised for mobile. As a novel approach, as there was no intention to evaluate different architectures and implementations, the criteria for choosing the neural network was its ease to use and no major dependence on set up parameters. The input

---

[7]the images were recorded in grayscale, containing only one channel

data was generated by splitting the image into two, to use each notch separately as an independent training data, following the statement that the failure initiates at only one of them, at peak load instant, the fractured side is used for training the *Fractured* class, for frames beyond initiation. After generating the stress components images, for each frame, the images were divided in training, separation, and validation, to avoid overfitting, that is, an excessively close fit to the training data. Then, the training data were input to the ConvNet as follows:

$$\text{Class}_f = \begin{cases} \text{Fratured} & \text{if } f < f_p \\ \text{Non-fractured} & \text{if } f \geq f_p \end{cases} \tag{3.22}$$

Chapter 4

Results and discussion

4.1 Subset size

After processing the images following the steps described in section 3. The speckle size and the nearest neighbours distributions were obtained (Figures 4.1 and 4.2).

(a) I.1.
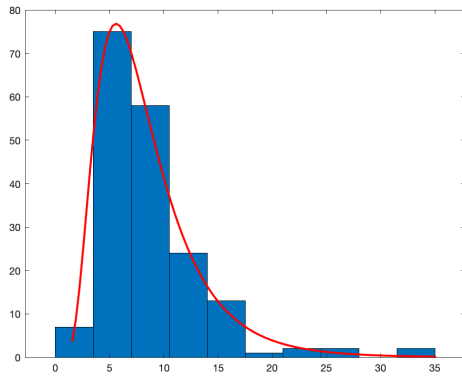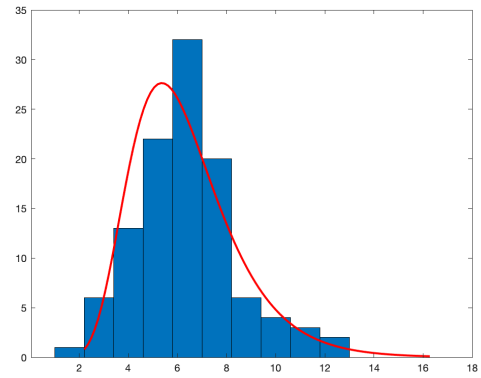
(b) II.1.
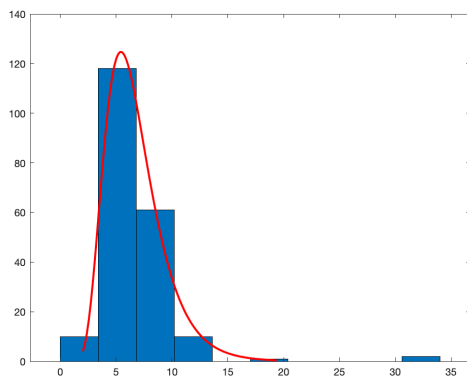
(c) III.1.
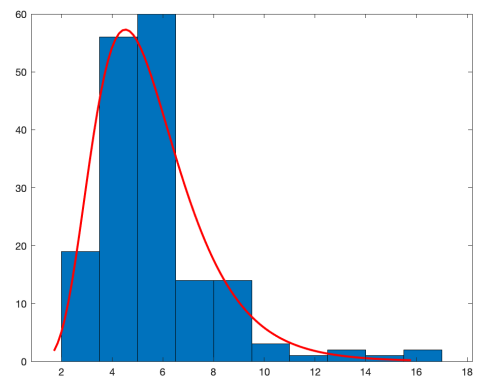
(d) IV.1.

Figure 4.1: Typical speckle size distribution, in px, from results.

(a) I.1.
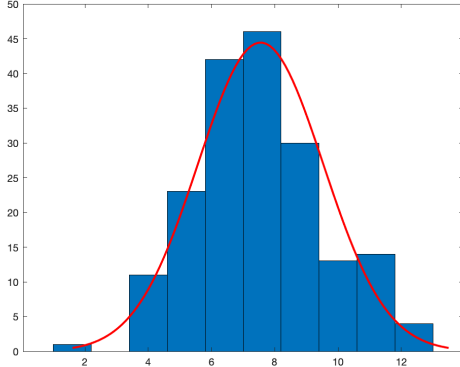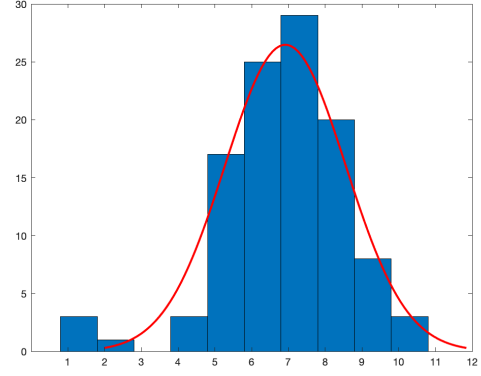
(b) II.1.
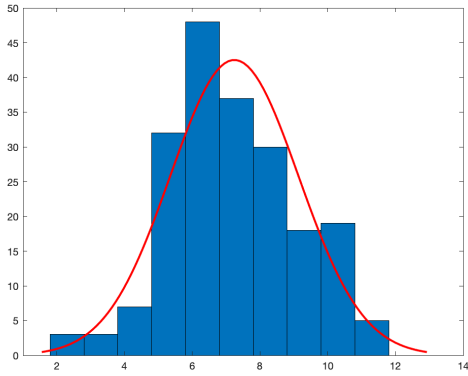
(c) III.1.
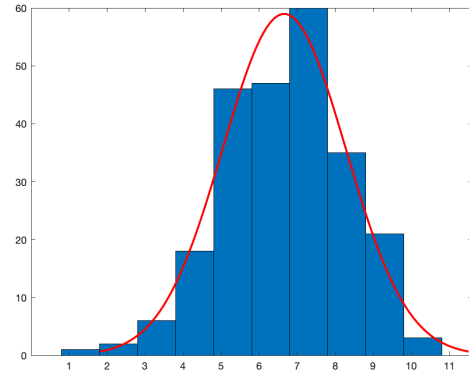
(d) IV.1.

Figure 4.2: Typical nearest neighbour distance distribution, in px, from results.

Despite of having the same resolution and similar dimensions in pixels, the geometric similar specimens have different (increasing) mm to px relation, which means that the same length in px, covers a longer distance in mm. Therefore, larger specimens show greater $SD_{95\%}$, $NND_{95\%}$, and consequently $2SR$, in mm even thought decreasing values in px, because of the *zoom out* effect, as shown in table 4.1). The subset model can be visually checked on figure 4.3. It shows that the proposed geometric model fulfil the criterion of number of speckles per subset.

Table 4.1: Results for subset size and input parameters, in px (mm)

	I.1	I.2	I.3	II.1	II.2	II.3	III.1	III.2	IV.1	IV.2	IV.3
$SD_{95\%}$	17	18	18	10	14	13	11	11	10	10	10
	(1.5)	(1.5)	(1.6)	(2.0)	(1.8)	(1.6)	(1.9)	(1.9)	(2.2)	(2.3)	(2.2)
$NND_{95\%}$	12	11	10	11	12	12	11	12	11	10	10
	(1.0)	(0.9)	(0.9)	(2.1)	(1.6)	(1.5)	(2.0)	(2.1)	(2.5)	(2.2)	(2.2)
$2SR$	15	15	15	11	14	13	12	12	11	11	11
	(1.3)	(1.3)	(1.3)	(2.2)	(1.8)	(1.7)	(2.1)	(2.1)	(2.5)	(2.5)	(2.5)

(a) I.1.   (b) II.2.

(c) III.2.   (d) IV.1.

Figure 4.3: Subset diameter example (white circle) for each class.

4.2 Dynamic fracture toughness

Figures 4.4 and 4.5 show the J-integral results against time for contour and area domain integrals, respectively. For the line integral the results are highly scattered compared to the area domain. Considering the nature of the loading, as an impact, the stress field are developed by the superposition of elastic waves moving along (and reflecting back) the specimen until it reaches the dynamic stress equilibrium, provoking an oscillatory-like stress pattern on stress fields that can be seen on figure 4.7.

In this scenario, the line integral acts like a fixed boundary in space capturing the elastic waves passing through, which could explain the highly scattered evolution over time. Differently, the area integral acts like a volume control, which the stress waves move within. As a result the oscillatory behaviour is homogenised, and the dispersion reduced, as shown in figure 4.5. Additionally, this is emphasised in figure 4.6, showing that the coefficient of determination is generally higher for the area domain calculations.

The results calculated by the area integral (Equation 3.10) are more consistent compared to contour domain (Equation 3.11). The robustness of the area domain strategy on calculating G_I time series can be an important argument for choosing the area method rather than the line integral. It is important to remark that equation 3.11 also contains an area domain term, but as will be further discussed, it is negligible for G_I calculation. Table 4.2 shows the G_{IC} values calculated by the area domain integral. Because its unsatisfactory results, the contour domain results will
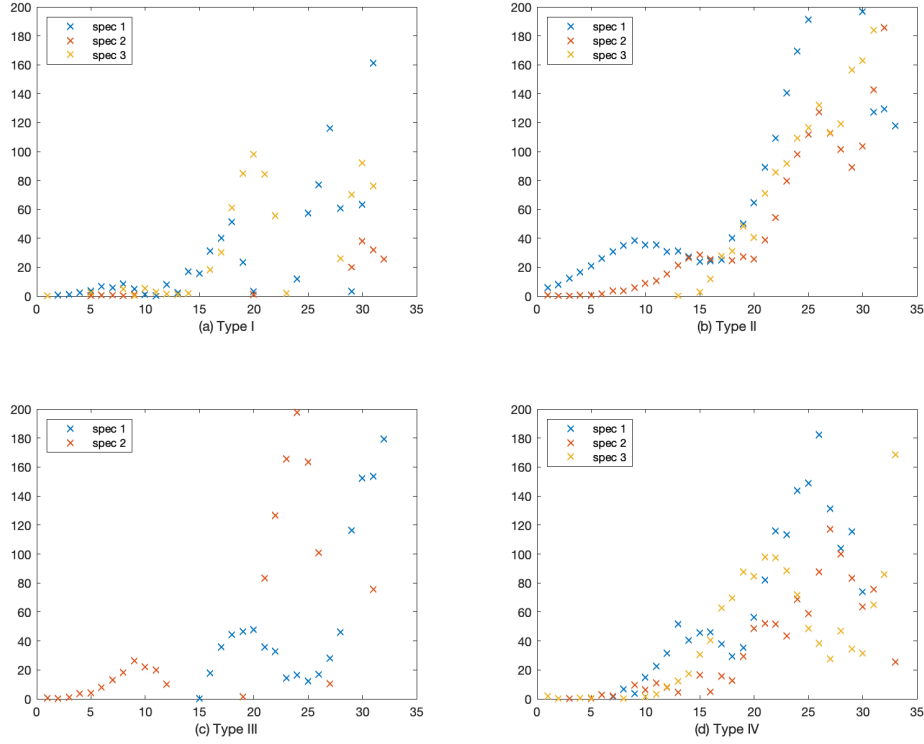
Figure 4.4: J-integral (kJ/m^2) *vs.* time $(frame)$ for contour domain.

not be further considered as an energy release rate measure, as such. Section 4.2.1 includes its results but only as a matter of comparison between the two strategies.

Table 4.2: G_{IC} results for $SW = 9, \gamma_i = 0,$ and $c = h = 90\%$ (kJ/m^2).

I.1	I.2	I.3	II.1	II.2	II.3	III.1	III.2	IV.1	IV.2	IV.3
81.68	18.31	47.85	60.54	55.32	64.04	109.11	206.15	119.34	23.29	55.56

4.2.1 Parameters sensitivity

Different sets of input parameters, described in section 3.3.2, have been tested as a measure of robustness of the method and path independence of the energy fields. The results relate to table 3.4. The four parameter variation applies only for the area domain. Despite of having an area integral in its formulation, the contour domain approach did not consider the inner contour factor γ_i as a parameter, since it only sums the inertial term contribution, that is negligible, its value was fixed to zero (meaning $\Gamma_i \to 0$).

Tables 4.5 and 4.4 show the coefficient of variation for the area and the line integral respectively. The high variability on the line integral results corroborates the statement that it is unsuitability for the G_I calculation under impact loads. For the

44
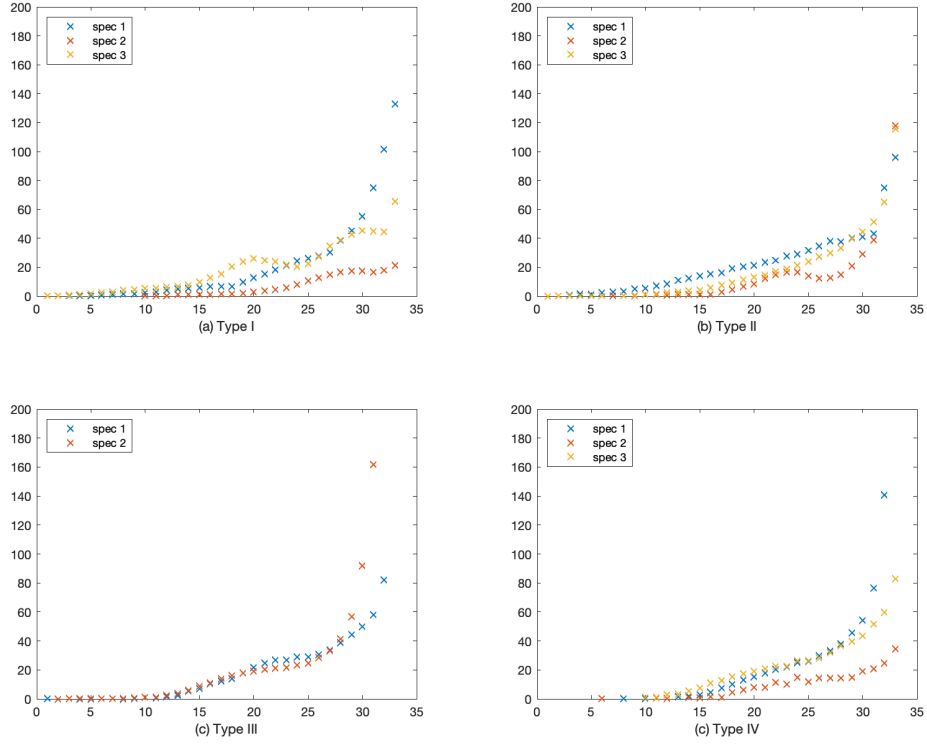
Figure 4.5: J-integral (kJ/m^2) *vs.* time ($frame$) for area domain.
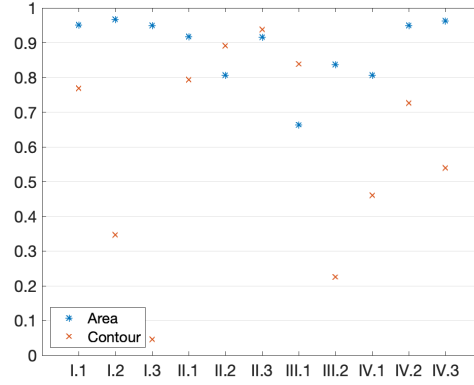
Figure 4.6: r^2 of J-integral polynomial regression for each specimen.

vast majority of the studied parameters combination it presented an unsatisfactory coefficient of variation meaning its lack of robustness regarding both the strain calculation and domain parameters.

In contrast, the use of the area domain mitigates the path dependence related to the elastic waves propagation and seems quite insensitive to parameters variation, for the studied range. The greater variation found is 14%, for II.1 specimen. This specimen has a particular low resolution ($128 \times 120px^2$) which could be the source of the variability, because of the lack of enough area to homogenise the energy fields,

(a) σ_{xx} field at $f_p - 10$ for IV.1 specimen's top notch.

(b) $\sigma_{xx}(MPa)$ over frames for a single datapoint near the notch.
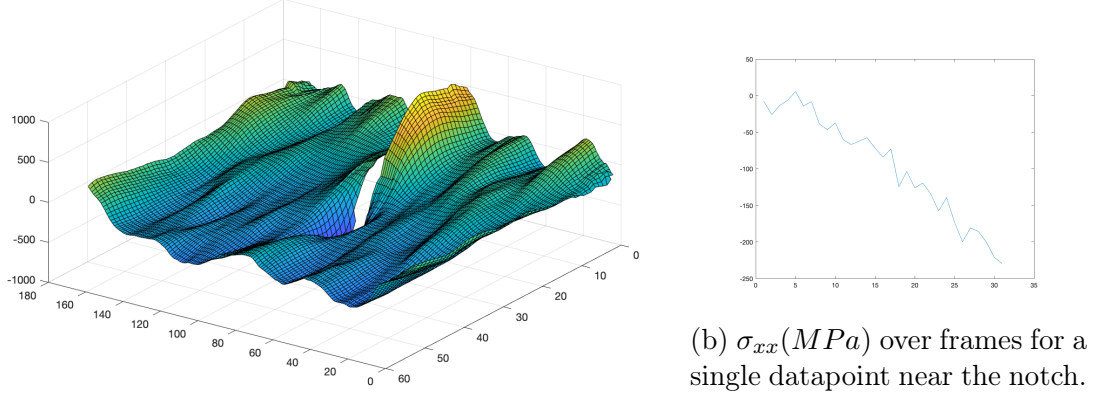
Figure 4.7: Oscillatory-like aspec of the stress field.

adding more weight to the path dependence caused by waves propagation. All the configurations have shown satisfactory coefficient of variation, what supports the use of the area integral on dynamic G_I calculation.

Table 4.3: Coefficient of variation (in %) of each specimen for results calculated by using the area domain integral.

	I.1	I.2	I.3	II.1	II.2	II.3	III.1	III.2	IV.1	IV.2	IV.3
4 par.	4.0	4.8	9.4	14.0	6.1	4.9	6.3	1.9	5.4	8.8	10.9
3 par.	4.8	3.7	8.4	12.5	5.6	5.7	5.7	3.3	6.0	9.2	9.4
2 par.	4.4	3.6	8.0	12.0	4.9	5.6	6.0	1.1	5.8	7.4	8.9
1 par.	5.2	3.5	0.4	9.8	4.5	5.5	1.0	1.2	3.7	0.7	5.1

Table 4.4: Coefficient of variation (in %) of each specimen for results calculated by using the line integral.

	I.1	I.2	I.3	II.1	II.2	II.3	III.1	III.2	IV.1	IV.2	IV.3
3 par.	50.8	70.8	42.7	28.6	38.2	59.4	15.2	7.9	19.9	48.2	37.3
2 par.	127.7	143.5	114.1	140.9	136.3	144.8	141.1	185.8	138.0	152.4	120.6
1 par.	5.7	45.6	42.8	36.3	54.6	30.9	19.0	16.5	21.9	143.3	11.2

4.2.2   Relative influence

The accuracy achieved by the neural network for fitting the data from table 4.5 was satisfactory. The results show an overall fitting accuracy of 99%. For a most generic fitting analysis, the achieved accuracy would represent overfitting, perhaps unsuitable for predicting outputs for different datasets. But in this specific case the aim is to map inputs and outputs for the given dataset and not to calibrate a

prediction model, so the high accuracy represents a good mapping between input and outputs.

Figure 4.9 shows a superposition of all specimens results in the parameters domain to show a general trend on their relative influence. It indicates that the domain width has the greatest influence on G_{IC} calculation amongst the other considered input parameters. Is supports the previously discussion about mitigating the path dependence caused by the elastic waves propagation by maximising the area domain, that is, for the same instant of time, a larger domain would be less sensitive to energy fields heterogeneity than smaller areas. In addition, the smaller the domain is, the greater the weight of the notch tip asymptomatic fields on the energy calculation.

The above arguments apply for both domain width and height, and no conclusion has been made on the the height being the most influence. It is not a major discussion to the topic here studied, the absolute values of energy variation indicates the robustness of the method and none of the individual variables can be remarked as having a special role in the G_{IC} calculation.
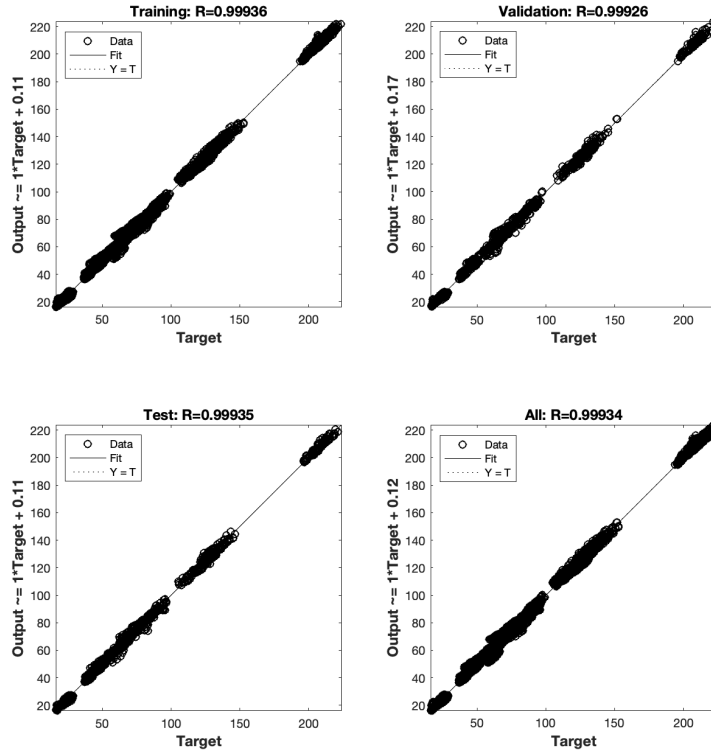
Figure 4.8: Neural network performance.

47
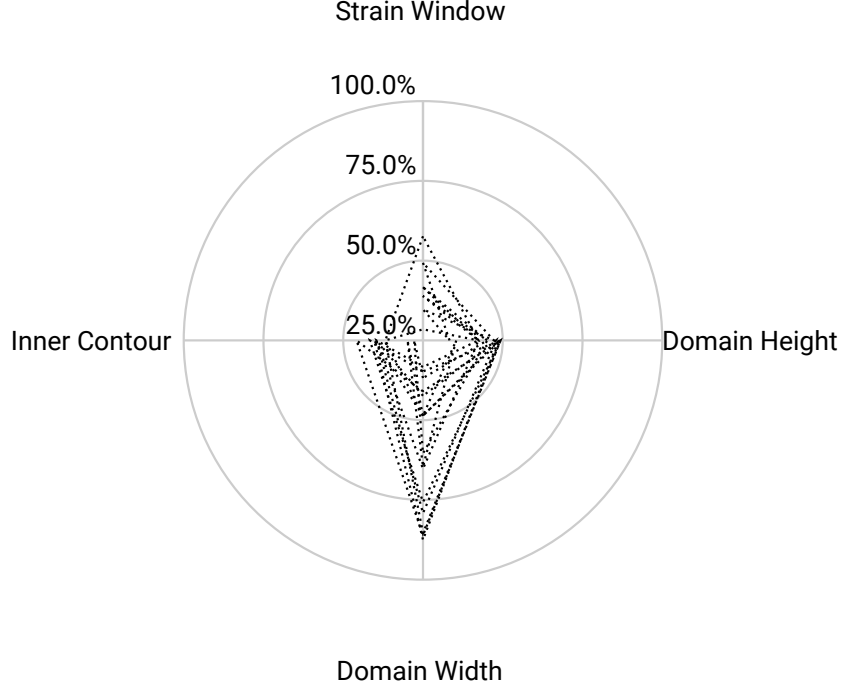
Figure 4.9: Parameters relative influence.

4.2.3 Inertial energy

The proposed methodology enables the assessment of the individual terms of the J-integral, clarifying whether the inertia effect is negligible or not. In the present case the results are negligible, reaching a maximum value of 0.7% of the total G_{IC} value (specimen IV.3). One may think it could be explained by the low density of the studied material. In a qualitative analysis it would be a plausible explanation. But as can be seen on equation 3.3.1, the inertial term varies linearly with the material density, which means that even for steel, five times heavier than the carbon composite, for the same displacement and acceleration fields, the value would not exceed 5.6% of the total G_{IC} value. What leaves the cause to the acceleration field imposed by the impact load. Even for $\dot{\epsilon} = 100s^{-1}$, it was not enough to generate a non negligible energy value.

Table 4.5: Area domain inertial term energy for $SW = 9, \gamma_i = 0,$ and $c = h = 90\%$ (kJ/m^2).

I.1	I.2	I.3	II.1	II.2	II.3	III.1	III.2	IV.1	IV.2	IV.3
0.04	0.01	0.03	0.16	0.07	0.07	0.29	0.25	0.37	0.38	0.42

4.2.4 R-Curve comparison

Following the same strategy as KUHN *et al.* [16] to obtain the theoretical abscissa Δa for each calculated G_{IC}, as described in section 3.3.3, it was possible to compare the obtained results with the R-curves calculated by KUHN *et al.* [16].

In figure 4.10a, the results are compared to both R-curves: quasi-static and dynamic. By analysing the plot, some statements can be made:

i The lack of consistency amongst specimens of the same Type becomes more evident when the results are plotted against Δa. When analysing the experimental results obtained by KUHN *et al.* [16] for the peak load σ_u, it does not fit as a plausible source of noise. Despite of G_{IC} relating quadratically to σ_u, the results do not go towards to same trend, what discards this hypothesis and leaves the explanation for a different source.

ii From the results for Type III specimens, with an average value of approximately $315kJ/m^2$, it is possible to draw some conclusions: besides the variation within the same specimen type, this particular specimen size could be put as an outlier compared to the other results, differing more than twice from the closest value, what does not happen amongst the other specimens. It could indicate a problem in the input values, not in the methodology itself. Taking into account that the method presented satisfactory robustness regarding the calculation parameters, with consistence results for the same input data, a possible source of error is a improper definition of the initiation frame, in other words, an unsynced relation between the loading history and the recorded images.

iii The proper identification of the initiation frame , or the peak-load frame, is crucial, and maybe, the more important input data of the whole methodology. Depending on the time resolution a ± 1 variation on the declared frame could lead to completely different conclusions. It opens a gap for a parallel field of study, that is the proper identification of the fracture initiation, based on the full-field measurement. In the next section a novel methodology is suggested as a field to be developed in the future, that uses convolutional neural networks on the proper fracture detection.

iv Finally, if only the average values are considered, excluding the outlier, the results show an increasing trend of G_{IC} value with Δa indicating a possible existence of the rising R-curve for the studied material. Additionally, the results are slightly closer to the dynamic R-curve, indicating the rate sensitivity of the fracture toughness. Assuming the later statement is true, a plausible

source of rate sensitivity would be a material level phenomenon instead of any kinematic contribution, as the acceleration, to the total energy calculation. It corroborates the rate sensitivity related to the occurrence of kink bands. Kink bands are well established as the common compression failure mechanism in carbon composites [61] and consist in localised change in the fibre orientation due to the presence to a compressive stress field. The formation of such structures depends on the adjacent support of the fibres to prevent the micro buckling of the fibres. Since this support is guaranteed by the polymeric matrix and it presents strain rate sensitivity, it could explain the rate sensitivity on the fracture toughness of such materials [62].

(a) Original results   (b) With Type III adjusted by ConvNet.
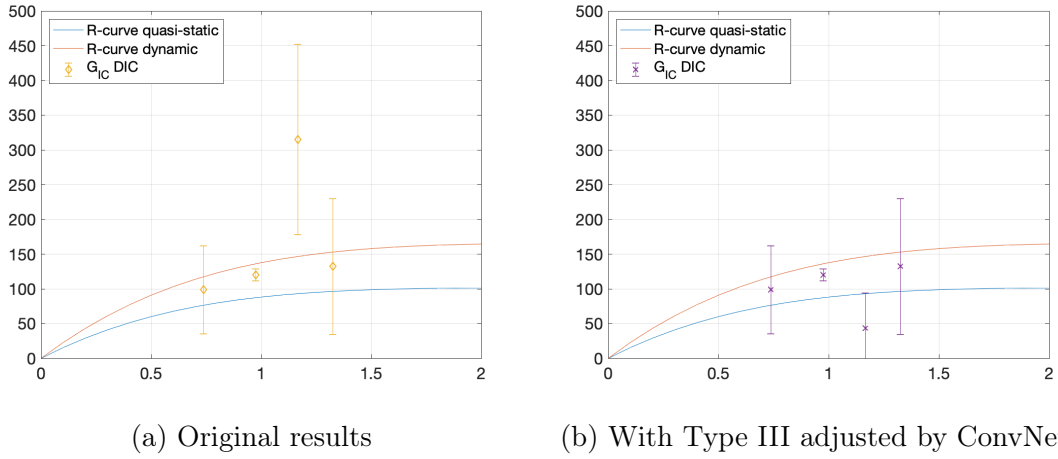
Figure 4.10: Comparison between G_{IC} (kJ/m^2) vs. Δa (mm) results and R-curves (the error bars stand for ± 1 standard deviation).

4.3 Initiation fracture toughness estimates by deep learning

4.3.1 Case study: *Type III specimens*

After training the convolutional neural network with Types I, II, and IV specimens, the network was applied to the Type III stress fields aiming to correct a supposed improper initiation frame. The overall training accuracy reached 98% and the results are shown in figure 3.3.4.

The results suggest that the likelihood of the fracture to have occurred, increases up to 1 (100%) several frames before the value obtained by the load-history curve. Approximately at the 20th and 19th frames for specimens III.1 and III.2 respectively. It reflects in a considerably reduction in the measured fracture toughness, as can

be seen in figure 4.10b. It suggests that the use of image classifiers on stress fields could be supporting tool on the proper fracture identification.
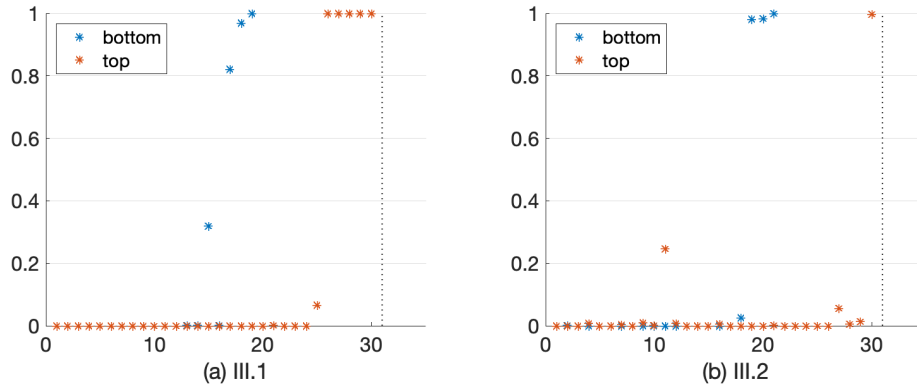
Figure 4.11: Likelyhood to belong to *Fractured* class *vs.* frame (the 31th frame corresponds to the peak-load, or instability initiation).

Chapter 5

Conclusion

In the present thesis a strategy for analysing the compressive fracture of carbon composites by digital image correlation is presented. The conclusions are summarised as follows:

i The proposed subset model allied to the analysis of the parameters influence indicates that the pre-processing step, that is, the measurement of the full-fields produced satisfactory results for the further calculations.

ii The use of the area integral rather than the contour domain has been shown to be the best for G_{IC} calculation under dynamic loads where the stress fields develop by the elastic wave propagation. The proposed method has shown satisfactory robustness due to the variation of the calculation parameters and seems to mitigate the path dependency under dynamically generated stress fields.

iii The proposed method revealed that the inertial term of the dynamic J-integral could be neglected in the present case.

iv An artificial neural network was successfully applied on the determination of the relative influence of the input parameters and has been shown as an alternative to traditional statistical techniques.

v On the other hand, the image analysis approach presented itself highly dependent on the accurate definition of the peak-load frame, leading to inconclusive results in cases where this information is doubtful.

vi The comparative results show a plausible occurrence of a rising R-curve, dependent on the strain-rate regime. But the lack of consistence does not strictly state such dependence, yet leaving an open point for discussion.

vii The application of convolutional neural networks on the stress fields of dynamically loaded specimens can be used as an efficient support tool for failure identification on composite materials.

Bibliography

[1] BLABER, J., ADAIR, B., ANTONIOU, A. "Ncorr: Open-Source 2D Digital Image Correlation Matlab Software", *Experimental Mechanics*, v. 55, 03 2015. doi: 10.1007/s11340-015-0009-1.

[2] KANNINEN, M. F., POPELAR, C. H. "Dynamic Fracture Mechanics". In: *Advanced Fracture Mechanics*, OUP USA, pp. 192–280, 1985.

[3] ANDERSON, T. L. "Dynamic and time-dependent fracture". In: *Fracture mechanics : fundamentals and applications*, CRC Press, pp. 173–212, 2005.

[4] JACOB, G. C., STARBUCK, J. M., FELLERS, J. F., et al. "Strain rate effects on the mechanical properties of polymer composite materials", *Journal of Applied Polymer Science*, v. 94, n. 1, pp. 296–301, set. 2004.

[5] FRACASSO, R., RINK, M., PAVAN, A., et al. "The effects of strain-rate and temperature on the interlaminar fracture toughness of interleaved PEEK/CF composites", *Composites Science and Technology*, v. 61, n. 1, pp. 57–63, jan. 2001.

[6] SUN, C., HAN, C. "A method for testing interlaminar dynamic fracture toughness of polymeric composites", *Composites Part B: Engineering*, v. 35, n. 6-8, pp. 647–655, set. 2004.

[7] WU, X. F., DZENIS, Y. A. "Determination of dynamic delamination toughness of a graphite-fiber/epoxy composite using hopkinson pressure bar", *Polymer Composites*, v. 26, n. 2, pp. 165–180, 2005.

[8] BLACKMAN, B., KINLOCH, A., RODRIGUEZ SANCHEZ, F., et al. "The fracture behaviour of structural adhesives under high rates of testing", *Engineering Fracture Mechanics*, v. 76, n. 18, pp. 2868–2889, 2009.

[9] BLACKMAN, B., KINLOCH, A., RODRIGUEZ-SANCHEZ, F., et al. "The fracture behaviour of adhesively-bonded composite joints: Effects of rate of test and mode of loading", *International Journal of Solids and Structures*, v. 49, n. 13, pp. 1434–1452, jun 2012. ISSN: 00207683.

[10] JOUDON, V., PORTEMONT, G., LAURO, F., et al. "Experimental procedure to characterize the mode I dynamic fracture toughness of advanced epoxy resins", *Engineering Fracture Mechanics*, v. 126, pp. 166–177, 2014.

[11] NAVARRO, P., AUBRY, J., PASCAL, F., et al. "Influence of the stacking sequence and crack velocity on fracture toughness of woven composite laminates in mode I", *Engineering Fracture Mechanics*, v. 131, pp. 340–348, 2014.

[12] ZABALA, H., ARETXABALETA, L., CASTILLO, G., et al. "Loading rate dependency on mode I interlaminar fracture toughness of unidirectional and woven carbon fibre epoxy composites", *Composite Structures*, v. 121, pp. 75–82, 2015.

[13] CANTWELL, W. J., BLYTON, M. "Influence of Loading Rate on the Interlaminar Fracture Properties of High Performance Composites - A Review", *Applied Mechanics Reviews*, v. 52, n. 6, pp. 199, 1999.

[14] REEDER, J. R., ALLEN, D. H., BRADLEY, W. L. "Effect of Elevated Temperature and Loading Rate on Delamination Fracture Toughness". In: *ICCM 14th International Conference on Composite Materials*, pp. 1–8, 2003.

[15] BEDSOLE, R. W., BOGERT, P. B., TIPPUR, H. V. "An experimental investigation of interlaminar and intralaminar dynamic fracture of CFRPs: Effect of matrix modification using carbon nanotubes", *Composite Structures*, v. 132, pp. 1043–1055, 2015.

[16] KUHN, P., CATALANOTTI, G., XAVIER, J., et al. "Fracture toughness and crack resistance curves for fiber compressive failure mode in polymer composites under high rate loading", *Composite Structures*, v. 182, n. September, pp. 164–175, 2017. ISSN: 02638223.

[17] KUHN, P., CATALANOTTI, G., XAVIER, J., et al. "Determination of the crack resistance curve for intralaminar fiber tensile failure mode in polymer composites under high rate loading", *Composite Structures*, v. 204, pp. 276–287, nov 2018. ISSN: 02638223.

[18] WOSU, S. N., HUI, D., DUTTA, P. K. "Dynamic mode II delamination fracture of unidirectional graphite/epoxy composites", *Composites Part B: Engineering*, v. 34, n. 3, pp. 303–316, abr. 2003.

[19] COLIN DE VERDIERE, M., SKORDOS, A., WALTON, A., et al. "Influence of loading rate on the delamination response of untufted and tufted car-

bon epoxy non-crimp fabric composites/Mode II", *Engineering Fracture Mechanics*, v. 96, pp. 1–10, 2012.

[20] WOSU, S. N., HUI, D., DUTTA, P. K. "Dynamic mixed-mode I/II delamination fracture and energy release rate of unidirectional graphite/epoxy composites", *Engineering Fracture Mechanics*, v. 72, n. 10, pp. 1531–1558, 2005.

[21] LEE, D., TIPPUR, H., BOGERT, P. "Quasi-static and dynamic fracture of graphite/epoxy composites: An optical study of loading-rate effects", *Composites Part B: Engineering*, v. 41, n. 6, pp. 462–474, 2010.

[22] BIE, B., HAN, J., LU, L., et al. "Dynamic fracture of carbon nanotube/epoxy composites under high strain-rate loading", *Composites Part A: Applied Science and Manufacturing*, v. 68, pp. 282–288, 2015.

[23] JIANG, F., VECCHIO, K. S. "Hopkinson Bar Loaded Fracture Experimental Technique : A Critical Review of Dynamic", *Applied Mechanics Reviews*, v. 62, n. November, 2009.

[24] NISHIOKA, T. "Computational dynamic fracture mechanics", *International Journal of Fracture*, v. 86, n. 1, pp. 127–159, 1997.

[25] D5528, A. S. *Standard Test Method for Mode I Interlaminar Fracture Toughness of Unidirectional Fiber-Reinforced Polymer Matrix Composites*. Relatório técnico, ASTM, 2013. www.astm.org.

[26] JIH, C. J., SUN, C. T. "Evaluation of a finite element based crack-closure method for calculating static and dynamic strain energy release rates", *Engineering Fracture Mechanics*, v. 37, n. 2, pp. 313–322, 1990.

[27] MALLUCK, J. F., KING, W. W. "Fast Fracture Simulated by Conventional Finite Elements: A Comparison of Two Energy-Release Algorithms", *ASTM STP711*, pp. 38–53, 1980.

[28] GUO, C., SUN, C. "Dynamic Mode-I crack-propagation in a carbon/epoxy composite", *Composites Science and Technology*, v. 58, n. 9, pp. 1405–1410, 1998.

[29] SIH, G. C., PARIS, P. C., IRWIN, G. R. "On cracks in rectilinearly anisotropic bodies", *International Journal of Fracture Mechanics*, v. 1, n. 3, pp. 189–203, 1965.

[30] BLACKMAN, B. R. K., DEAR, J. P., KINLOCH, A. J., et al. "The failure of fibre composites and adhesively bonded fibre composites under high rates of test - Part I Mode I loading-experimental studies", *Journal of Materials Science*, v. 30, n. 23, pp. 5885–5900, 1995.

[31] LEE, D., TIPPUR, H., KIRUGULIGE, M., et al. "Experimental Study of Dynamic Crack Growth in Unidirectional Graphite/Epoxy Composites using Digital Image Correlation Method and High-speed Photography", *Journal of Composite Materials*, v. 43, n. 19, pp. 2081–2108, 2009. ISSN: 0021-9983.

[32] LIU, C., ROSAKIS, A. J., STOUT, M. G. "Dynamic Fracture Toughness of a Unidirectional Graphite / Epoxy Composite". In: *Proceedings of the Symposium on Dynamic Effects in Composite Structures*, New York, 2001. ASME.

[33] KHANNA, S., SHUKLA, A. "On the use of strain gages in dynamic fracture mechanics", *Engineering Fracture Mechanics*, v. 51, n. 6, pp. 933–948, 1995.

[34] GRADY, D. "The spall strength of condensed matter", *Journal of the Mechanics and Physics of Solids*, v. 36, n. 3, pp. 353–384, 1988.

[35] BAŽANT, Z., PLANAS, J. *Fracture and Size Effect in Concrete and Other Quasibrittle Materials*. CRC Press, 1998.

[36] CATALANOTTI, G., XAVIER, J., CAMANHO, P. P. "Measurement of the compressive crack resistance curve of composites using the size effect law", *Composites Part A: Applied Science and Manufacturing*, v. 56, pp. 300–307, 2014. ISSN: 1359835X.

[37] CATALANOTTI, G., ARTEIRO, A., HAYATI, M., et al. "Determination of the mode I crack resistance curve of polymer composites using the size-effect law", *Engineering Fracture Mechanics*, v. 118, pp. 49–65, mar 2014. ISSN: 00137944.

[38] CATALANOTTI, G., XAVIER, J. "Measurement of the mode II intralaminar fracture toughness and R-curve of polymer composites using a modified Iosipescu specimen and the size effect law", *Engineering Fracture Mechanics*, v. 138, pp. 202–214, mar 2015. ISSN: 00137944.

[39] SUTTON, M., WOLTERS, W., PETERS, W., et al. "Determination of displacements using an improved digital correlation method", *Image and Vi-*

sion Computing, v. 1, n. 3, pp. 133–139, aug 1983. ISSN: 02628856. doi: 10.1016/0262-8856(83)90064-1.

[40] PAN, B., QIAN, K., XIE, H., et al. "Two-dimensional digital image correlation for in-plane displacement and strain measurement: a review", *Measurement Science and Technology*, v. 20, n. 6, pp. 062001, jun 2009. ISSN: 0957-0233. doi: 10.1088/0957-0233/20/6/062001.

[41] ROUX, S., RÉTHORÉ, J., HILD, F. "Digital image correlation and fracture: an advanced technique for estimating stress intensity factors of 2D and 3D cracks", *Journal of Physics D: Applied Physics*, v. 42, n. 21, pp. 214004, 2009. ISSN: 0022-3727.

[42] KIRUGULIGE, M. S., TIPPUR, H. V., DENNEY, T. S. "Measurement of transient deformations using digital image correlation method and high-speed photography: application to dynamic fracture." *Applied optics*, v. 46, n. 22, pp. 5083–5096, 2007. ISSN: 0003-6935.

[43] CATALANOTTI, G., CAMANHO, P., XAVIER, J., et al. "Measurement of resistance curves in the longitudinal failure of composites using digital image correlation", *Composites Science and Technology*, v. 70, n. 13, pp. 1986–1993, nov 2010. ISSN: 02663538.

[44] BECKER, T. H., MOSTAFAVI, M., TAIT, R. B., et al. "An approach to calculate the J-integral by digital image correlation displacement field measurement", *Fatigue & Fracture of Engineering Materials & Structures*, v. 35, n. 10, pp. 971–984, oct 2012. ISSN: 8756758X.

[45] HOU, F., HONG, S. "Characterization of R-curve behavior of translaminar crack growth in cross-ply composite laminates using digital image correlation", *Engineering Fracture Mechanics*, v. 117, pp. 51–70, feb 2014. ISSN: 00137944.

[46] GAO, G., YAO, W., XIA, K., et al. "Investigation of the rate dependence of fracture propagation in rocks using digital image correlation (DIC) method", *Engineering Fracture Mechanics*, v. 138, pp. 146–155, apr 2015. ISSN: 00137944.

[47] ALLAER, K., DE BAERE, I., VAN PAEPEGEM, W., et al. "Direct fracture toughness determination of a ductile epoxy polymer from digital image correlation measurements on a single edge notched bending sample", *Polymer Testing*, v. 42, pp. 199–207, apr 2015. ISSN: 01429418.

[48] KOERBER, H., XAVIER, J., CAMANHO, P. "High strain rate characterisation of unidirectional carbon-epoxy IM7-8552 in transverse compression and in-plane shear using digital image correlation", *Mechanics of Materials*, v. 42, n. 11, pp. 1004–1019, nov 2010. ISSN: 01676636.

[49] KOERBER, H., CAMANHO, P. P. "High strain rate characterisation of unidirectional carbon-epoxy IM7-8552 in longitudinal compression", *Composites Part A: Applied Science and Manufacturing*, v. 42, n. 5, pp. 462–470, may 2011. ISSN: 1359835X.

[50] "Material Data Sheet". 2013. HexPly 8852 Product Data.

[51] LI, J., FOK, A. S., SATTERTHWAITE, J., et al. "Measurement of the full-field polymerization shrinkage and depth of cure of dental composites using digital image correlation", *Dental Materials*, v. 25, n. 5, pp. 582–588, may 2009. ISSN: 01095641. doi: 10.1016/j.dental.2008.11.001.

[52] SCHNEIDER, C. A., RASBAND, W. S., ELICEIRI, K. W. "NIH Image to ImageJ: 25 years of image analysis", *Nature Methods*, v. 9, pp. 671, jun 2012.

[53] BERNSEN, J. "Dynamic thresholding of gray-level images". In: *Proceedings - International Conference on Pattern Recognition*, 1986.

[54] ATLURI, S. N. "Path-independent integrals in finite elasticity and inelasticity, with body forces, inertia, and arbitrary crack-face conditions", *Engineering Fracture Mechanics*, v. 16, n. 3, pp. 341–364, jan 1982. ISSN: 0013-7944.

[55] KUNA, M. "Basics of Fracture Mechanics". In: *Finite Elements in Fracture Mechanics: Theory - Numerics - Applications*, pp. 21–151, Dordrecht, Springer Netherlands, 2013. ISBN: 978-94-007-6680-8. doi: 10.1007/978-94-007-6680-8_3.

[56] OLDEN, J. D., JACKSON, D. A. "Illuminating the 'black box': a randomisation approach for understanding variable contributions in artificial neural networks", *Ecological Modelling*, v. 154, n. 1-2, pp. 135–150, aug 2002. ISSN: 03043800. doi: 10.1016/S0304-3800(02)00064-9.

[57] LONDRES, G. "Determination of composite materials resistance curves under dynamic strain rates". 2017. Undergraduate Project, Poli/UFRJ.

[58] MOREL, S., DOURADO, N. "Size effect in quasibrittle failure: Analytical model and numerical simulations using cohesive zone model", *International Journal of Solids and Structures*, v. 48, n. 10, pp. 1403–1412, 2011. ISSN: 00207683. doi: 10.1016/j.ijsolstr.2011.01.014.

[59] KRIZHEVSKY, A., SUTSKEVER, I., HINTON, G. E. "ImageNet Classification with Deep Convolutional Neural Networks", *Commun. ACM*, v. 60, n. 6, pp. 84–90, maio 2017. ISSN: 0001-0782. doi: 10.1145/3065386.

[60] HOWARD, A. G., ZHU, M., CHEN, B., et al. "MobileNets: Efficient Convolutional Neural Networks for Mobile Vision Applications", *CoRR*, v. abs/1704.04861, 2017.

[61] NARAYANAN, S., SCHADLER, L. S. "Mechanisms of kink-band formation in graphite/epoxy composites: a micromechanical experimental study", *Composites Science and Technology*, v. 59, n. 15, pp. 2201–2213, 1999. ISSN: 02663538. doi: 10.1016/S0266-3538(99)00074-3.

[62] HAHN, H., WILLIAMS, J. "Compression Failure Mechanisms in Unidirectional Composites". In: *Composite Materials: Testing and Design (Seventh Conference)*, ASTM International, pp. 115–115–25, 100 Barr Harbor Drive, PO Box C700, West Conshohocken, PA 19428-2959. doi: 10.1520/STP35345S.

Appendix A

Related Publication

Determination of mode I dynamic fracture toughness of IM7-8552 composites by digital image correlation and machine learning

Rafael A. Cidade[a,*], Daniel S.V. Castro[a], Enrique M. Castrodeza[a,b], Peter Kuhn[c], Giuseppe Catalanotti[d], Jose Xavier[e,f], Pedro P. Camanho[e,g]

[a] Department of Metallurgical and Materials Engineering, COPPE Federal University of Rio de Janeiro, P.O. Box 68505, 21941-972 Rio de Janeiro, Brazil
[b] Department of Mechanical Engineering, Politecnico di Milano, Via La Masa 1, 20156 Milano, Italy
[c] Department of Mechanical Engineering, Chair for Carbon Composites, Technical University of Munich, Boltzmannstraße 15, Garching, Germany
[d] Advanced Composites Research Group (ACRG), School of Mechanical and Aerospace Engineering, Queen's University Belfast, Belfast BT9 5AH, UK
[e] Instituto de Ciência e Inovação em Engenharia Mecânica e Engenharia Industrial, Rua Dr. Roberto Frias, 400, 4200-465 Porto, Portugal
[f] UNIDEMI, New University of Lisbon, Faculty of Sciences and Technology, Department of Mechanical and Industrial Engineering, Campus de Caparica, Caparica 2829-516, Portugal
[g] DEMec, Faculdade de Engenharia, Universidade do Porto, Rua Dr. Roberto Frias, s/n, 4200-465 Porto, Portugal

ARTICLE INFO

ABSTRACT

An optical experimental procedure for evaluating the J-Integral from full-field displacement fields under dynamic loading is proposed in this work. The methodology is applied to measure the J-integral in the dynamic compressive loading of fiber-reinforced composites and to calculate the dynamic fracture toughness associated with the propagation of a kink-band. A modified J-Integral that considers inertia effects is calculated over the full-field measurements obtained by digital image correlation, for double edge-notched specimen of IM7-8552 laminates dynamically loaded in a split-Hopkinson pressure bar (SHPB). A sensibility study is conducted to address the influence of the speckle parameters. The results show good agreement with experimental observations obtained by using a different data reduction method, suggesting the existence of a rising R-curve for the studied material under dynamic loading. Furthermore, it was noticed that the inertia effect can be negligible, indicating a state of dynamic equilibrium in which quasi-static approaches may comfortably be used.

1. Introduction

The compression failure in notched composites has been thoroughly studied with during the past decades [1–5]. Fiber-reinforced composites exhibit in compression a failure mechanism through the onset and propagation of kink bands [6,2,7,8] that may be represented as cracks. Therefore, a fracture toughness is associated to the kink band failure mechanism. The fracture toughness is one of the key parameters used in strength prediction methods for composite materials. Its accurate determination is therefore essential and has given birth, in the past years, to the widespread development of different experimental techniques.

The experimental work performed has been mainly conducted under static loading conditions. The CT specimen ([9–11], among others) and the size effect method [12] have been used to measure the R-curve associated with the propagation of a kink-band. Despite the work performed so far only one paper [13] has been published on the determination of dynamic compressive failure for fiber-reinforced composites. Considering that, in several real applications, composite structures need to withstand dynamic loading, it is necessary to further understand the dynamic behavior of this important class of materials.

Several works have studied the strain-rate dependence on fracture toughness of composite materials. Changes in the fracture toughness value have been explained by rate dependence on elastic properties as well as sensitivity of stress resistance limit [13–17]. This indicates a lack of consensus regarding the origin of the time dependent behavior, motivating effort toward this topic.

Many authors rely on quasi-static approaches on data reduction of their dynamic analysis, relying on the premise that dynamic stress equilibrium has been reached. Jiang and Vecchio [18] show in a review that the quasi-static theory is the preferred method to calculate fracture toughness under impact conditions, a conclusion reached by many other authors [19–23]. On the other hand, Nishioka [24] considers that the use of computer simulations is the only possible way to overcome difficulties in acquiring higher-order dynamic properties along a

---

* Corresponding author.
E-mail address: rafaelcidade@poli.ufrj.br (R.A. Cidade).

<div style="border: 1px solid black; padding: 10px;">

List of symbols

E_x, E_y, G_{xy}	longitudinal, transversal, and shear modulus
v_{xy}	in-plane Poisson coefficient
W	specimen half width
a, a_0, Δa	crack length, initial crack length, crack increment
$\dot{\epsilon}$	strain rate
SR	subset radius
NND	nearest neighbor distance
D	Feret diameter
J^d, j^d_{fit}	dynamic J-Integral, dynamic J-Integral fit
u, $\ddot{u}$	displacement field, acceleration field
x	in-plane direction
U	elastic energy
δ	Kronecker delta
σ	stress tensor
ρ	specific mass
q	weight function
A	area of a data point
dp	data point
c, h	domain width, domain height
Γ_i	inner contour region
G_C, G_{C0}, G_{C90}	laminate fracture toughness and fracture toughness of 0° and 90° plies
t, t_p	time frame, peak load time frame
$RI_\%$	variable relative importance
I_{ij}	input-hidden layer connection weights
Z_j	hidden layer-output connection weights
l, l_0	laminate thickness, thickness of 0° plies

</div>

transient loading history.

Sun and Han [25] used the modified crack closure (MCC) integral to calculate mode I dynamic energy release rate of wedge loaded compact tension (WLCT) specimens using a finite elements formulation suggested by Jih and Sun [26]. The crack propagation is simulated by sequentially releasing the crack path nodes, based on experimental measurements of crack tip position, and the crack-closure integral calculated continuously trailing the crack-tip [27]. For Jih and Sun [26], an advantage of this method compared to the J-Integral is that it can easily separate the energy release rate for each fracture mode without knowing, *a priori*, the mixed-mode ratio. Navarro et al. [28] followed the work of Guo and Sun [29], which similarly to Sun and Hun [25], used the finite elements method with node releasing strategy to calculate mode I dynamic fracture toughness of carbon/epoxy and glass/epoxy composites. Differently from Jih and Sun [26], they used the energy balance (total strain-energy and total kinetic-energy) to calculate the energy release rate. Wu and Dzenis [30] also performed finite elements simulations on their dynamic delamination (Modes I and II) study. Instead of using a contour integral, like in the work presented by Sun and Han [25], they calculated stress intensity factors directly by the crack opening displacement, assuming an asymptotic displacement field near crack tip (Sih et al. [31]). The use of the crack opening displacement instead of J-Integral was justified by the fact that the numerical differentiation step would reduce the accuracy of the analysis, since the stress field is calculated by the displacement derivative. In addition, it was pointed out that the dynamic path-independent integral would not avoid the singular stress field because it involves area integrals within the contour. Lee et al. [32] used the analytical expressions of the displacement field derived by Liu et al. [33] to calculate the dynamic stress intensity factor. Differently from Wu and Dzenis [30], where finite elements method was employed do calculate the crack opening displacement, they used 2D digital image correlation (DIC) and high-speed photography to obtain the full-field displacements and further calculate the dynamic stress intensity factors. An analogous approach was used by Joudon et al. [34] for the measurement of the dynamic mode I fracture toughness of toughened epoxy resins. The authors used a strain gage method instead of DIC, following the work of Khanna and Shukla [35], which assumes an asymptotic strain field near the tip of a moving crack with constant velocity. Additionally, the authors mentioned that the local analysis of asymptotic fields are preferred on determining fracture mechanics parameters during fast propagating cracks on brittle polymers. Kunh et al. [13] studied the dynamic compression toughness for carbon/epoxy under a strain rate of $100\,s^{-1}$. The approach presented uses the relations between the size effect law, proposed by Bažant et al. [36], the energy release rate and R-curve, under a quasi-static assumption, reporting a significant increase in the fracture toughness. In agreement with Wosu et al. [21], they reported a negligible influence of the kinetic energy in total process

energy, justifying the use of the quasi-static approach.

The use of J-Integral over full-field measurements has also been proposed. Jiang et al. [37] calculated the value of the J-Integral, under quasi-static regime, for composite materials used in dental restorations over full-field measurements obtained by DIC and reported no considerable dependence on size and location of the integration path, concluding that the J-Integral calculation aside the DIC, is a reliable technique for calculating the material fracture toughness. Similar results were found in other studies, confirming the reliability of the use of J-Integral over full-field measurements [38,39 9]. In addition, the use of the area domain J-Integral has been reported by some authors as an advantageous alternative to the traditional contour J-Integral, regarding the integration domain dependency and the error reduction [40,41].

To achieve a reliable DIC, the subset size must be trade-off between the capacity of distinguishing it from different subsets and avoiding mask heterogeneities in full-field measurements by using a large window. Additionally, small subsets would lead to an increase of local correlation coefficient minimums, decreasing the technique efficiency [42]. Studies have been done towards finding the optimal subset values, considering the image and the speckle pattern properties. A practical suggestion is the use of a subset size that circumscribes at least three speckle particles. Leading to the development of geometric models for determining the optimal subset size [43–49].

However, all the studies performed using J-Integral and DIC were done in quasi-static conditions and didn't evaluated the J results sensitivity in relation to the parameters used in DIC and in the formulation of J-Integral, although there are some works that evaluate the influence of DIC parameters in strain error. Thus, this work aims to analyse, by using artificial neural networks, the influence of the parameters used for J calculation. In addition, it is discussed the application of an inertial term in the J integral and the possibility of the construction of a dynamic R curve based on fracture toughness results.

This work is complementary to the published by Kuhn et al. [13]. Therefore, it is discussed the determination of the dynamic fracture toughness of the tested material by two different methodologies: the analytical model presented by Catalanotti et al. [9,12], and the DIC analysis, proposed in this paper.

2. Materials and methods

2.1. Material and tests specimens.

Flat panels with a 4 mm thickness and a layup of $[90/0]_{8S}$ were manufactured using HexPly IM7-8552 carbon-epoxy prepreg system. The panel was cured by hot-pressing following the curing cycle suggested by the manufacturer [50]. Table 1 shows the elastic properties of the laminate measured under high strain ($\dot{\epsilon} = 100s^{-1}$) [13].

Table 1
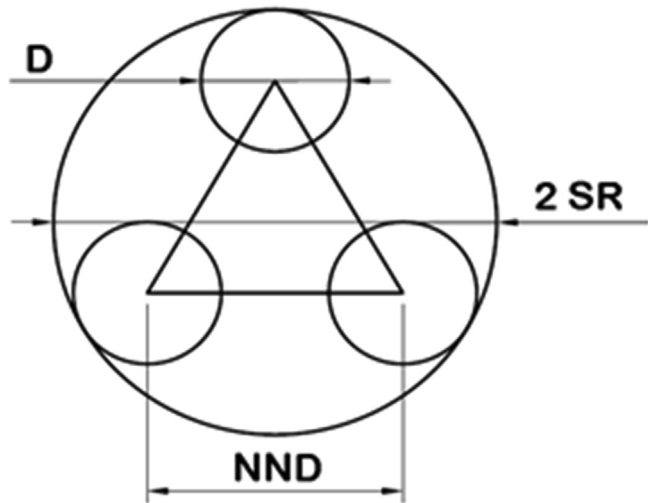Laminate elastic properties for high strain rate.

$E_x = E_y$ (GPa)	G_{xy} (GPa)	ν_{xy}
67.126	6.345	0.04
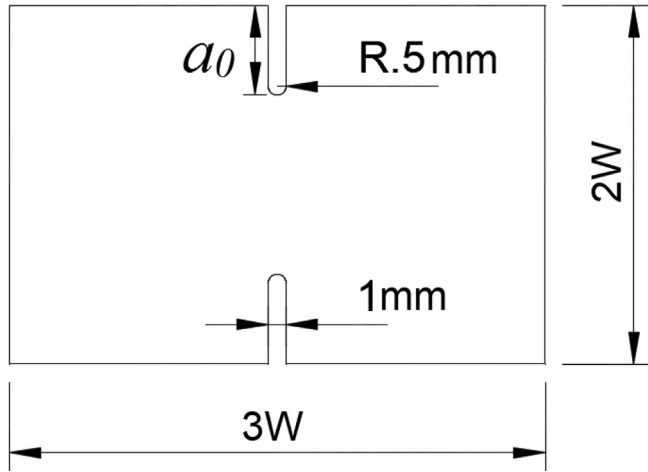
Fig. 1. Specimen geometry.

Table 2
Nominal dimensions of the specimens (all values in mm).

Specimen type	I	II	III
a_0	2.50	3.75	6.75
W	5.00	7.50	12.50

Fig. 2. Geometric model for subset radius.

High strain rate fracture tests were carried out on double-edge notched in compression (DENC) specimens machined from the panel by a 1 mm drill bit. The specimens have all the same shape but different sizes, or in other word, the width and the length of the specimen are proportional to a characteristic size, W, as indicated in Fig. 1. Table 2 shows the dimensions used in this experimental campaign.

For the assessment of full-field displacements by the DIC technique the specimens were covered by a random black and white speckle pattern.

2.2. Experimental setup and high strain rate tests

The high strain rate tests were performed in a split-Hopkinson pressure bar (SHPB). Different bar diameters and pulse shapers were used to achieve the same strain rate for all specimens ($\dot{\epsilon} = 100 s^{-1}$). A high-performance PHOTRON AS-Z camera was used to capture the speckle pattern variation along time. The acquisition frequency and the resolution were 300,000 fps 256×128 pixels^2, respectively. Further details of the experimental setup can be found in [13].

3. Full field measurements (DIC)

3.1. Subset determination model

Aiming for a good analysis of deformations by the DIC method, the ideal size of the subset radius to be used must be determined. It will determine the size of the window for which the occurred displacement identification is made according to the change of location of sets of points at different gray scale values. In order to respect the requirements of having at least 3 speckles by subset [48] and to ensure the best possible resolution, a geometric model, in which the speckles are considered perfectly circular and their centers are located at the vertices of an equilateral triangle, is proposed. This is the most homogeneous arrangement for three points around the same reference point. Therefore, the model considers the distance between the centers of the circles as the nearest neighbor distance (NND) and that the diameter of the circles as the speckles Feret diameter (D) [51], as shown in Fig. 2.

The considered value for the speckle size is that which covers 95% of the particles Feret diameter distribution, ensuring a wide range of particles size within the subset. Analogously, the free path between particles considered is that in respect of 95% of the nearest neighbor distance distribution (NND). By using Euclidian geometry, the subset radius value (SR), that is equivalent to de distance between de triangle center and the circumference that circumscribes the three small circles, is calculated by Eq. (1).

$$SR = D_{95\%} + NND_{95\%} \frac{\sqrt{3}}{3} \tag{1}$$

To obtain the speckles Feret diameter and the free path distributions, image processing techniques were performed in steps, illustrated in Fig. 3, using the open source software ImageJ® [52], following the sequence below:

a) Histogram equalization: To enhance the contrast by stretching out the intensity distribution to the whole range of intensity spectrum.
b) Classification: The image is made binary by using the Bernsen adaptive threshold filter [53], with a 15×15 px^2 window. The resulting black regions refer to the particles while white regions refer to the background.
c) Watershed: to avoid overestimating the particles size by separating touching objects.
d) Area filter and despeckle: To remove particles smaller than 4 px^2 and smooth sharp regions of particles.

3.2. Full field measurements

The full field measurements (displacements and strains) were calculated by the DIC technique, using the open-source DIC software Ncorr [42]. The subset size for each specimen was determined by the procedure descripted previously. Green-Lagrange strains are calculated by Ncorr, using the strain-displacement relation with small deformation formulation (Eq. (2)). Ncorr uses piecewise least-squares fitting over a region of the displacement field data points, the strain window, to calculate the displacements gradient (∇u). The size of the strain window will be discussed further.
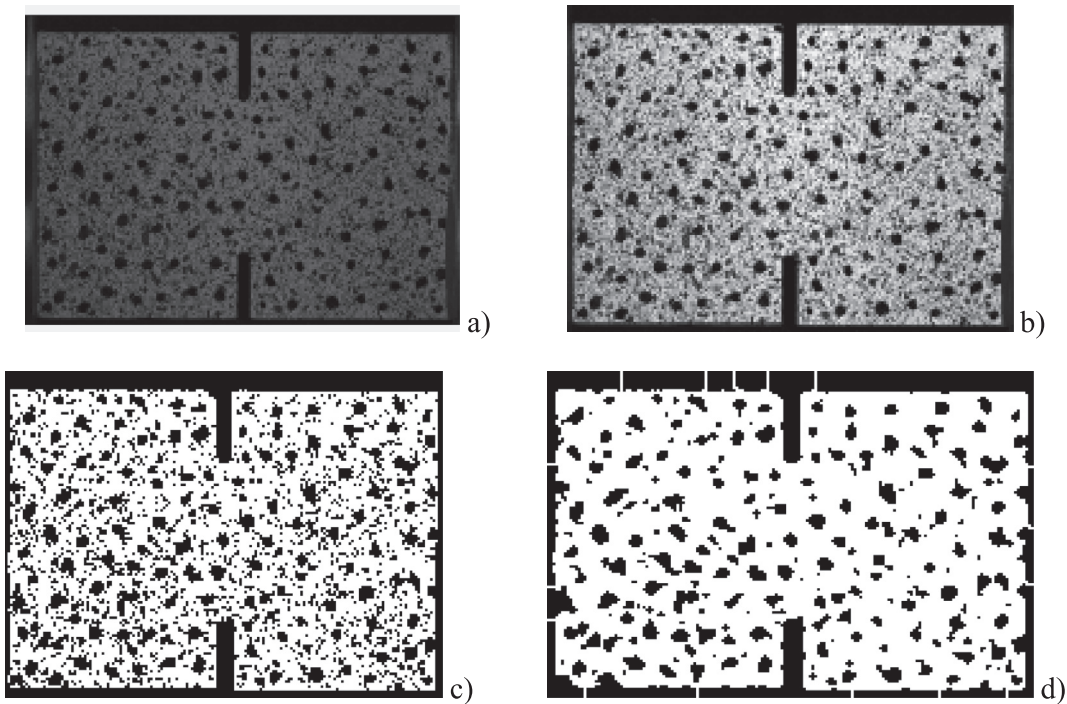
Fig. 3. a) Original image; b) Equalized image; c) Binary image; and d) Final image after watershed and size filtering.
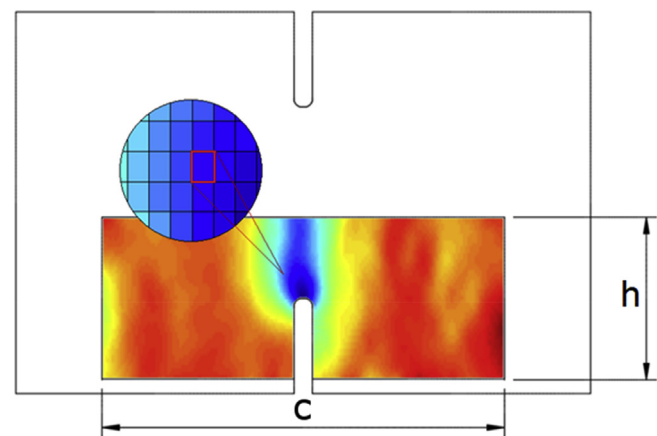

Fig. 4. An illustration of a stress field within a domain of size $c \times h$ including the notch, showing a single data point, marked in red.
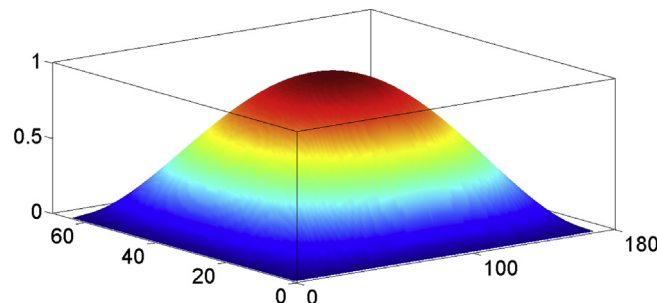

Fig. 5. Weight function for a 170×65 data points domain.
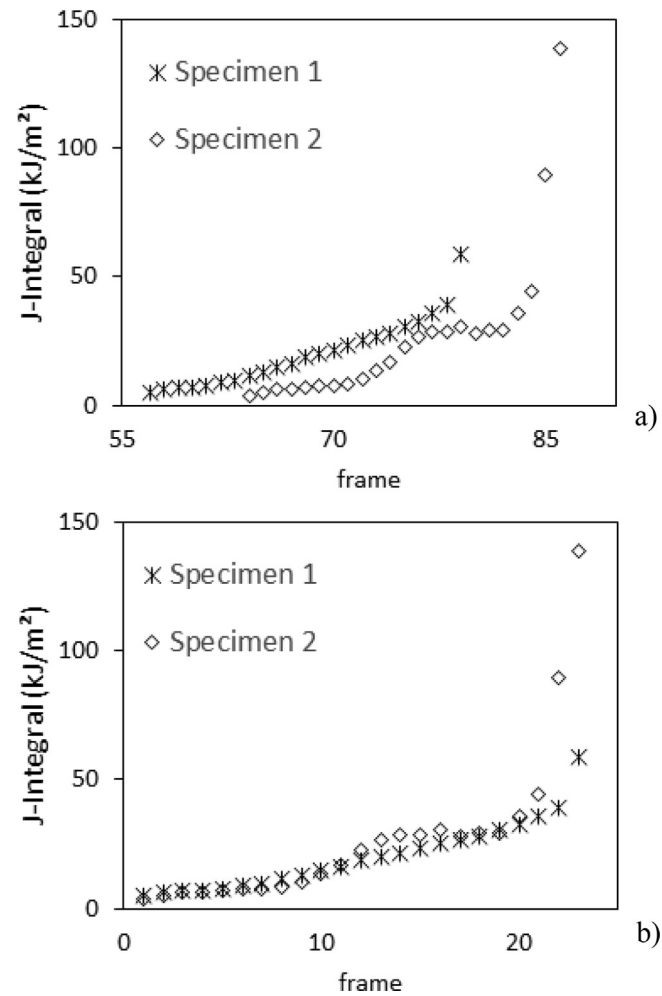

Fig. 6. J-Integral scatter over time frames, (a) original input data, (b) shifted to synchronize the peak load frame.

Table 3
Parameters and parameter levels of the full factorial design.

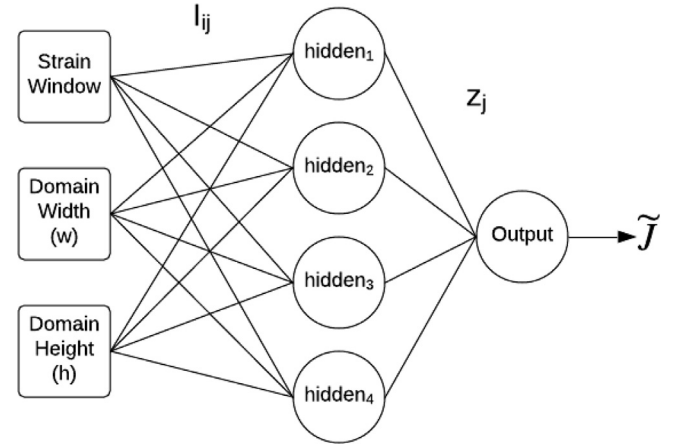| Parameter	Level 1	Level 2	Level 3	Level 4	Level 5
Strain window (data points)	10	14	18	22	26
Domain height	50%	60%	70%	80%	90%
Domain width	50%	60%	70%	80%	90%

Fig. 7. Diagram of the multilayer perceptron used for $RI_\%$ estimates.

Table 4
Results for the subset size for each specimen type (all values in pixels).

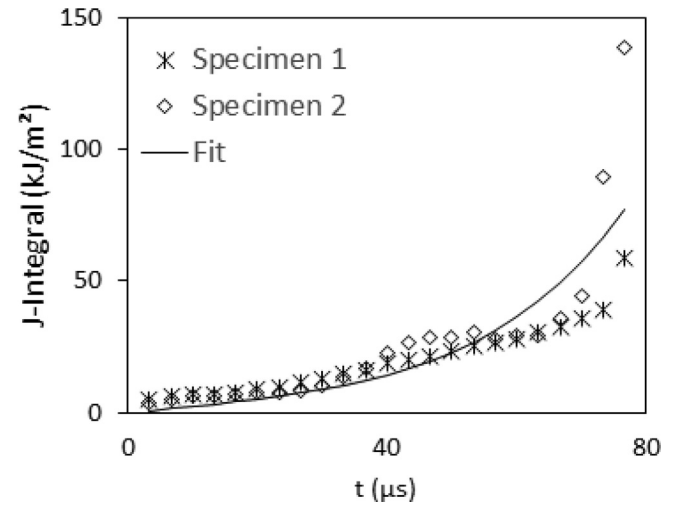| Specimen type	D	NND	SR
I	17 ± 1	11 ± 1	15 ± 0
II	12 ± 2	11 ± 1	13 ± 4
III	10 ± 1	10 ± 1	11 ± 2

Fig. 8. J-Integral over time for type II.

$$\epsilon = \frac{1}{2}\left(\frac{\Delta u_i}{\Delta x_j} + \frac{\Delta u_j}{\Delta x_i}\right) \tag{2}$$

4. Dynamic J-Integral calculation

4.1. Formulation

In this study an implementation of the J-Integral proposed by Atluri [54] and used in Kuna [55] is proposed. It considers the inertia effect
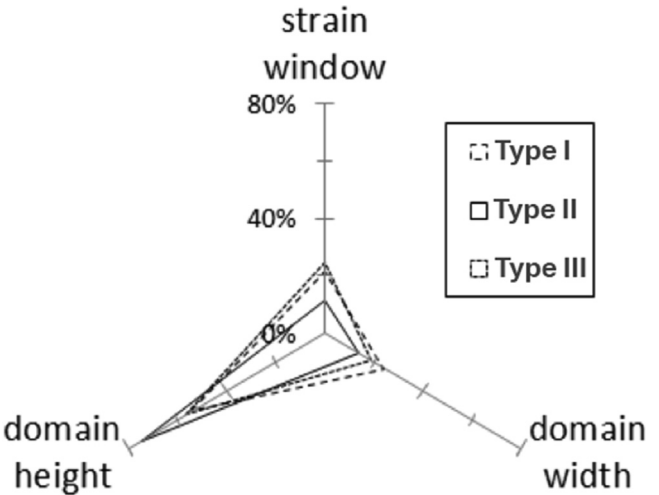

Fig. 9. Relative influence of variables on fracture toughness.

Table 5
Mean fracture toughness results and standard deviation (in kJ/m^2) regarding the variation of the factorial design parameters.

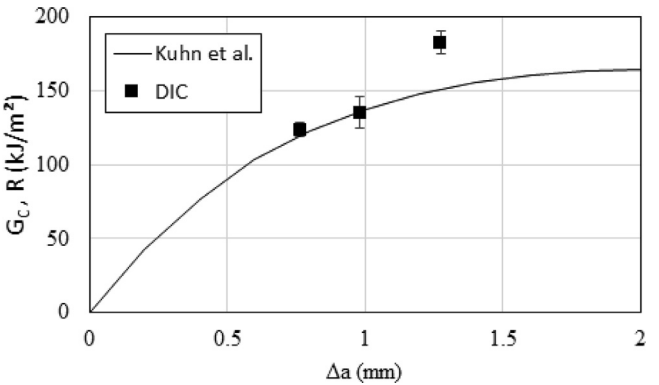| Specimen type	3 parameters	2 parameters	1 parameter
I	61.8 ± 2.4	61.7 ± 1.3	59.4 ± 1.2
II	67.6 ± 5.3	68.6 ± 3.4	66.4 ± 3.9
III	91.3 ± 4.0	91.6 ± 2.7	88.4 ± 3.0

Fig. 10. G_C points obtained in the present work (DIC) and the R-Curve obtained by Kuhn et al. [13] for longitudinal plies.

Table 6
Comparison of the determined fracture toughness value for IM7-8552 longitudinal plies with previous works.[1]

Author	Regime	G_C (kJ/m^2)
Present study (DIC)	$\dot{\epsilon} = 100 s^{-1}$	$\approx 120 - 180$
Kuhn et al. [13]	$\dot{\epsilon} = 100 s^{-1}$	≈ 165
Kuhn et al. [13]	Quasi-static	≈ 101
Catalanotti et al. [12]	Quasi-static	≈ 61

[1] The values related to Kuhn et al. [13] and Catalanotti et al. [12] refer to the steady-state fracture toughness value.

and neglects the kinetic energy, for the case of dynamically loaded stationary cracks.

The J-Integral is calculated for each notch, and the higher value is taken. The discrete implementation of the J-Integral is the sum of the contribution of each individual data point within the domain boundaries and A represents the area of a data point, in mm^2.

$$J^d = \sum_{dp} \left\{ \left[\left(U\delta_{i2} - \sigma_{i2}\frac{\Delta u_i}{\Delta x_2} \right) \frac{\Delta q}{\Delta x_j} + \rho\frac{\Delta u_i}{\Delta x_j}\ddot{u}_i q \right] A \right\}_{dp} \tag{3}$$

The domain transformation, from contour to area, requires the use of a weight function q, that must follow two requirements:

1. Must vary smoothly from 0 (at the outer contour) to 1 (at the inner contour).
2. Must value 1 within the inner contour (in the present case the inner contour $\Gamma_i \to 0$).

In the discrete implementation, the operator $\Delta/\Delta x_j$ represents the gradient vector, where Δx is the length represented by a data point edge. The J-Integral was calculated for every time step (i.e. image frames), so that a behavior over time can be obtained. The chosen function is a biquadratic equation, shown in Eq. (4), which satisfies the mentioned conditions.

$$q(x, y) = \left(\frac{c^2 - x^2}{c^2} \right) \left(\frac{h^2 - y^2}{h^2} \right) \tag{4}$$

In the proposed methodology the weight function is also responsible for the domain boundaries determination. Since it only has values within the outer contour and the J-Integral terms multiply q and ∇q, the J-Integral area domain can be set by the parameters c and h (i.e. the width and the height of function domain). Fig. 5 shows the biquadratic equation for a domain with 170×65 data points.

4.2. Fracture toughness definition

In this study, the initiation fracture toughness is defined as the point of instability, assumed as the point of the peak load during the test [13,12]. Considering the linear-elastic behavior of the material, G_C is defined as:

$$G_C = J^d|_{t=t_p} \tag{5}$$

The fracture toughness calculation consisted in a polynomial fit of the J-Integral values over time for all specimens of each type. A window of 23 consecutive frames, which comprises all the experimental fracture process, was used. The 21st frame matches the peak load time ($t = t_p$), so all specimens of each type could be synchronized by the peak load frame and plot over the same time domain, as can be seen on Fig. 6. Further, a third order polynomial was used to fit the J-Integral over time and the value of $J^d_{fit}|_{t=t_p}$ is assumed to be the initiation fracture toughness.

5. Parameters sensitivity analysis

The influence of three parameters were assessed in this study: the strain window, the domain width (c), and the domain height (h), as shown in Fig. 4.

5.1. Full factorial design

A full factorial design was generated to evaluate de influence of the parameters on J-Integral value. Three parameters were chosen for assessing the robustness of the method: the strain window, the domain height, and the domain width.

- The strain window relates to the sensitivity of the J-Integral regarding the smoothness of the strain field.
- The domain size variation verifies whether the area domain J-Integral is dependent to the integration domain, analogous to the path independence of the classic J-Integral.

Five levels, shown in Table 3, were heuristically chosen for each parameter.

5.2. Analysis of parameters relative importance ($RI_\%$)

Lilliefors' tests [56] have shown that the J-Integral residuals do not fit in a normal distribution regarding the variation of the parameters. So, it would not be appropriate to evaluate the effect of the variables using the ANOVA method. The connection weights (CWM) method was used to estimate RI for each variable based on the weights of a trained artificial neural network (ANN) [57]. The relative importance of a given input variable can be defined by Eq. (6), for the case of a single hidden layer.

$$RI_i = \sum_{h=1}^{n} I_{ij} Z_j \tag{6}$$

where, n is the total number of hidden nodes, I_{ij} is the weight of the connections between input nodes and hidden nodes, and Z_j is the weight of the connection between hidden nodes and the output node. In this study, a multilayer perceptron (MLP) ANN with four hidden neurons within a single hidden layer (Fig. 7) was heuristically chosen to evaluate the $RI_\%$ of input variables.

6. Results and discussion

6.1. Subset size

Table 4 shows the results for the subset size for each specimen type, and its respective input parameters (Feret diameter and NND).

The scale factor increases with the decrease of the specimen size (i.e. the zoom in smaller specimens has great magnitude compared to larger specimens), therefore all specimens present approximately the same size in pixels. Considering the speckle particles distribution to be the same for all specimens (the same application method was used), Larger specimens are expected to present smaller speckle particles, in pixels. Consequently, decreasing subset size.

6.2. Dynamic fracture toughness

The above defined initiation fracture toughness criterion was applied to all specimens. Fig. 8 shows the J-Integral over time and the polynomial fit for type II. The initial point, or 0 s, refers to the 20th frame before the peak load frame. It is a representative curve that follows the other types.

Computing the fracture toughness for all specimens, it was possible to evaluate the sensitivity of its value regarding the variation of the method parameters. The connection weights method [57] indicates that the greatest relative influence comes from the domain height (i.e. along crack direction), as shown in Fig. 9.

Table 5 shows the fracture toughness and its standard deviation for three scenarios:

- 3 parameters variation: the full factorial design.
- 2 parameters variation: strain window fixed at a value of 9 data points, and the domain parameters varying from 50% to 90% of the specimen size in the respective direction.
- 1 parameter variation: strain window fixed at a value of 9 data points, the domain width fixed at 90% of specimen width, varying the domain height from 50% to 90% of the specimen half height (W).

The results show an increasing trend of the dynamic fracture toughness in respect of specimen size. Considering that different sizes relate to different notch sizes (a_0), it is plausible the existence of a rising R-Curve for the IM7-8552 under dynamic loads, as expected. Since the R-Curve of a given material is invariant, in the present case in which $a_0/$

W is constant greater test specimens are expected to achieve instability at greater G_C values. This result agrees to the results obtained by Kuhn et al. [13], which calculated a R-curve of the same material based on the method proposed by Catalanotti et al. [12]. This method relies on the relation between the energy release rate and the size-effect law established by Bažant et al. [36].

The method used by Kuhn et al. [13] to establish the relation between W and Δa was applied to the results obtained in the present paper. Fig. 10 shows the average initiation fracture toughness of the full factorial design (Fig. 8) and the R-curve obtained by Kuhn et al. [13].

The R-Curve calculated by Kuhn et al. [13], for longitudinal plies, was compared to the fracture toughness results calculated in the present work (Eqs. (5) and (7)), neglecting the transversal plies contribution ($G_{C0} \gg G_{C90}$), following Pinho et al. [10].

$$G_{C0} = \frac{l}{l_0} G_C \qquad (7)$$

An important remark is that, differently from Kuhn et al. that obtained the R-Curve based on the size effect law applied on the specimens' ultimate stress, the present work calculates the G_C values based on full-field measurements, without using load information (except for the peak load time frame, t_p). The close agreement of the results indicates that the proposed methodology could be a reliable alternative for fracture toughness determination of composite laminates subjected to dynamic loads. Table 6 shows a comparison to values found in previous works for the same tested material. The same consideration of longitudinal fracture toughness applies (Eq. (7)).

Regarding the domain dependence on fracture toughness value (Table 5) the greatest variation coefficient is 7.8%, for the type II in full factorial scenario. It shows that the dynamic fracture toughness does not depend significantly on the chosen area domain.

6.3. Inertia effect

The fracture toughness calculation applied in this work (Eq. (3)), allows the assessment of the inertial term $\left(\rho \frac{\Delta u_i}{\Delta x_j} \ddot{u}_i q \right)$ contribution on total J-Integral value. It was found that the inertia contribution is negligible for all analyzed specimens, approximately 0.01%, 0.10%, and 0.35% of the total fracture toughness, for types I, II and, III respectively, suggesting the achievement of the dynamic equilibrium, agreeing with Kuhn et al. [13] on the reliability of the quasi-static methodology for the dynamic analysis. Moreover, a rising trend can be observed indicating the larger the specimens, the higher the inertial term is, even though it is negligible in the present study. This trend could be related to the time to achieve the dynamic equilibrium, that is longer for larger specimens [58].

7. Conclusions

The main conclusions outlined in this study can be summarized as follows:

- The modified J-Integral calculated in this study makes possible the evaluation whether the dynamic equilibrium have been achieved, by the analysis of the inertial term against the total energy release rate value.
- The proposed methodology for measuring the J-integral from full-field displacement provided by DIC is shown to be stable with regard to setting parameters. The results show a small variation coefficient regarding the DIC and the integration domain parameters.
- Machine learning was useful on assessing the relative influence of the input variables. The use of the weights of a trained artificial neural network was an alternative in the present case, where statistical distributions could not be applied.
- The results show a rising trend on the fracture toughness in respect

of the increase of the specimen size, and consequently the increase of a_0, suggesting the existence of a rising R-curve.
- Present results and those from Kuhn et al. [13] are in close agreement, even though they come from two different methodologies, with non-related input variables.

References

[1] Vogler TJ, Kyriakides S. On the axial propagation of kink bands in fiber composites: Part I experiments. Int J Solids Struct 1999;36(47):557–74.

[2] Budiansky B, Fleck NA. Compressive failure of fibre composites. J Mech Phys Solids 1993;41(1):183–211.

[3] Vogler TJ, Kyriakides S. On the initiation and growth of kink bands in fiber composites: Part I. Experiments. Int J Solids Struct 2001;38(15):2639–51.

[4] Hsu SY, Vogler TJ, Kyriakides S. Compressive strength predictions for fiber composites. ASME J Appl Mech 1998;65:7–16.

[5] Kyriakides SK, Arseculeratne R, Perry EJ, Liechti KM. On the compressive failure of fiber reinforced composites. Int J Solids Struct 1995;32:689–738.

[6] Patel J. Mechanisms for kink band evolution in polymer matrix composites: a digital image correlation and finite element study; 2016.

[7] Argon A. Fracture of composites. Treatise Mater Sci Technol 1972;1:79–114.

[8] Moran P, Shih C. Kink band propagation and broadening in ductile matrix fiber composites: experiments and analysis. Int J Solids Struct 1998;35(15):1709–22.

[9] Catalanotti G, Marques AT, Dávila CG, Xavier J, Camanho PP. Measurement of resistance curves in the longitudinal failure of composites using digital image correlation. Compos Sci Tachnol 2010;70(13):1986–93.

[10] Pinho ST, Robinson P, Iannucci L. Fracture toughness of the tensile and compressive fibre failure modes in laminated composites. Compos Sci Technol 2006;66:2069–79.

[11] Prasad MS, Venkatesha C, Jayaraju T. Experimental methods of determining fracture toughness of fiber reinforced polymer composites under various loading conditions. J Minerals Mater Char Eng 2011;10(13):1263–75.

[12] Catalanotti G, Xavier J, Camanho PP. Measurement of the compressive crack resistance curve of composites using the size effect law. Compos A Appl Sci Manuf 2014;56:300–7.

[13] Kuhn P, Koerber H, Catalanotti G, Xavier J, Camanho PP. Fracture toughness and crack resistance curves for fiber compressive failure mode in polymer composites under high rate loading. Compos Struct 2017;182(15):164–75.

[14] Hsiao HM, Daniel I. Strain rate behavior of composite materials. Composites Part B 1998;29(5):521–33.

[15] Bing Q, Sun CT. Modeling and testing strain rate-dependent compressive strength of carbon/epoxy composites. Compos Sci Technol 2005;65(15–16):2481–91.

[16] Koerber H, Camanho PP. High strain rate characterisation of unidirectional carbon–epoxy IM7-8552. Composites Part A 2011;42(11):462–70.

[17] Yokoyama T, Nakai T. Impact compressive failure of a unidirectional carbon/epoxy laminated composite in three principal material directions. In: Proceedings of DYMAT 2009 conference, Brussels; 2009.

[18] Jiang F, Vecchio KS. Hopkinson bar loaded fracture experimental technique: a critical review of dynamic. Appl Mech Rev 2009;62(6).

[19] Fracasso R, Rink M, Pavan A, Frassine R. The effects of strain-rate and temperature on the interlaminar fracture toughness of interleaved PEEK/CF composites. Compos Sci Technol 2001;61(1):57–63.

[20] Wosu SN, Hui D, Dutta PK. Dynamic mode II delamination fracture of unidirectional graphite/epoxy composites. Composites Part B 2003;34(3):303–16.

[21] Wosu SN, Hui D, Dutta PK. Dynamic mixed-mode I/II delamination fracture and energy release rate of unidirectional graphite/epoxy composites. Eng Fracture Mech 2005;72(10):1531–58.

[22] Colin de Verdiere M, Skordos AA, Walton AC, May M. Influence of loading rate on the delamination response of untufted and tufted carbon epoxy non-crimp fabric composites/Mode II. Eng Fract Mech 2012;96:1–10.

[23] Zabala H, Aretxabaleta L, Castillo G, Aurrekoetxea J. Loading rate dependency on mode I interlaminar fracture toughness of unidirectional and woven carbon fibre epoxy composites. Compos Struct 2015;121:75–82.

[24] Nishioka T. Computational dynamic fracture mechanics. Int J Fract 1997;86(1–2):127–59.

[25] Sun CT, Han C. A method for testing interlaminar dynamic fracture toughness of polymeric composites. Composites Part B 2004;35(6–8):647–55.

[26] Jih CJ, Sun CT. Evaluation of a finite element based crack-closure method for calculating static and dynamic strain energy release rates. Eng Fract Mech 1990;37(2):313–22.

[27] Malluck JF, King WW. Fast fracture simulated by conventional finite elements: a comparison of two energy-release algorithms, ASTM STP711; 1980. p. 38–53.

[28] Navarro P, Aubry J, Pascal F, Marguet S, Ferrero JF, Dorival O. Influence of the stacking sequence and crack velocity on fracture toughness of woven composite laminates in mode I. Eng Fract Mech 2014;131:340–8.

[29] Guo C, Sun CT. Dynamic Mode-I crack-propagation in a carbon/epoxy composite. Compos Sci Technol 1998;58(9):1405–10.

[30] Wu XF, Dzenis Ya. Determination of dynamic delamination toughness of a graphite-fiber/epoxy composite using Hopkinson pressure bar. Polym Compos 2005;26(2):165–80.

[31] Sih GC, Paris PC, Irwin GR. On cracks in rectilinearly anisotropic bodies. Int J Fract Mech 1965;1(3):189–203.

[32] Lee D, Tippur H, Bogert P. Quasi-static and dynamic fracture of graphite/epoxy composites: an optical study of loading-rate effects. Compos B Eng 2010;41(6):462–74.

[33] Liu C, Rosakis AJ, Stout MG. Dynamic fracture toughness of a unidirectional graphite/epoxy composite. In: Proceedings of the symposium on dynamic effects in composite structures, New York; 2001.

[34] Joudon V, Portemont G, Lauro F, Bennani B. Experimental procedure to characterize the mode I dynamic fracture toughness of advanced epoxy resins. Eng Fract Mech 2014;126:166–77.

[35] Khanna SK, Shukla A. On the use of strain gages in dynamic fracture mechanics. Eng Fract Mech 1995;51(6):933–48.

[36] Bazant Z, Kim JH, Daniel IM, Becq-Giraudon E, Zi G. Size effect on compression strength of fiber composites failing by kink band propagation. Int J Fract 1999;95:103–41.

[37] Jiang Y, Akkus A, Roperto R, Akkus O, Li B, Lang L, Teich S. Measurement of J-integral in CAD/CAM dental ceramics and composite resin by digital image correlation. J Mech Beh Biomed Mater 2016;62:240–6.

[38] Gonzáles GLG, González JAO, Castro JTP, Freire JLF. A J-integral approach using digital image correlation for evaluating stress intensity factors in fatigue cracks with closure effects. Theor Appl Fract Mech 2017;90:14–21.

[39] Allaer K, Baere ID, Paepegem WV, Degrieck J. Direct fracture toughness determination of a ductile epoxy polymer from digital image correlation measurements on a single edge notched bending sample. Polym Test 2015;42:199–207.

[40] Li FZ, Shih CF, Needleman A. A comparison of methods for calculating energy release rates. Eng Fract Mech 1985;21(2):405–21.

[41] Becker TH, Mostafavi M, Tait RB, Marrow TJ. An approach to calculate the J-integral by digital image correlation displacement field measurement. Fatigue Fract Eng Mater Struct 2012;35(10):971–84.

[42] Huang Y. Development of digital image correlation method for displacement and shape measurement, Singapore; 2004.

[43] Zhang J, Jin GC, Ma SP, Meng LB. Application of an improved subpixel registration algorithm on digital speckle correlation measurement. Optics Laser Tech 2003;35(7):533–42.

[44] Lecompte D, Smitsb A, Bossuytb S, Solb H, Vontommea J, Hemelrijck DV, et al. Quality assessment of speckle patterns for digital image correlation. Opt Lasers Eng 2006;44(11):1132–45.

[45] Sun YPH, Sun YF, Pang HL. Study of optimal subset size in digital image correlation of speckle pattern images. Optics Lasers Eng 2007;45(9):967–74.

[46] Haddadi HÃ, Belhabib S. Use of rigid-body motion for the investigation and estimation of the measurement errors related to digital image correlation technique. Opt Lasers Eng 2008;46(2):185–96.

[47] Lionello G, Cristofolini L. A practical approach to optimizing the preparation of speckle patterns for digital-image correlation. Meas Sci Technol 2014;25.

[48] Kasvayee KA, Elmquist L. Development of a pattern making method for strain measurement on microstructural level in ferritic cast iron. Process Fabricat Adv Mater 2014.

[49] Sutton MA, Orteu JJ, Schreier HW. Image correlation for shape and deformation measurements: basic concepts, theory and applications. New York, NY: Springer; 2009.

[50] Material Data Sheet. HexPly 8852 Product Data; 2013.

[51] Merkus HG. Particle size measurements: fundamentals, practice, quality. Springer; 1999.

[52] Schneider CA, Rasband WS, Eliceiri KW. NIH Image to ImageJ: 25 years of image analysis. Nat Methods 2012;9(7):671–5.

[53] Bernsen J. Dynamic thresholding of grey-level images. In: Proc. 8th International Conference on Pattern, Paris, 1986.

[54] Atluri SN. Path-indepent integrals in finite elasticity and inelasticity, with body forces, inertia and arbitrary crack-face conditions. Eng Fract Mech 1982;16(3):341–64.

[55] Kuna M. Finite elements in fracture mechanics. Netherlands: Springer; 2013.

[56] Lilliefors HW. On the Kolmogorov-Smirnov test for normality with mean and variance unknown. J Am Stat Assoc 1967;62(318):399–402.

[57] Olden JD, Jackson DA. Illuminating the "black box": a randomization approach for understanding variable contributions in artificial neural networks. Ecol Model 2002;154(1–2):135–50.

[58] Al-Maliky NS. Dimension effect on dynamic stress equilibrium in SHPB tests. Int J Mater Phys 2014;5(1):15–26.